Check for updates

Advanced Intelligent Systems

ADVANCED INTELLIGENT SYSTEMS Open Access

www.advintellsyst.com

RESEARCH ARTICLE OPEN ACCESS

i-Tac: Inverse Design of 3D-Printed Tactile Elastomers with Tuneable Optical and Mechanical Properties

Wen Fan | Dandan Zhang

Department of Bioengineering, Imperial College London, London, UK

Correspondence: Dandan Zhang (d.zhang17@imperial.ac.uk)

Received: 26 September 2025 | **Revised:** 24 March 2026 | **Accepted:** 25 March 2026

Keywords: elastomer manufacturing | inverse design | multi-objective optimisation | vision-based tactile sensor

ABSTRACT

Elastomers play a crucial role in capturing tactile information for vision-based tactile sensors (VBTSs), where they transduce contact stimuli into elastic deformation. Different sensor architectures demand distinct elastomer properties, such as optical transparency and mechanical hardness. Conventional forward design approaches, however, rely on iterative trial-and-error processes from material preparation to final performance, making them inefficient and difficult to scale. Here, we present i-Tac, an inverse design pipeline for tailoring the optical and mechanical properties of elastomers used in VBTSs. Inspired by the composite structure of the human dermis, i-Tac leverages multi-material additive manufacturing with three distinct PolyJet 3D printing resins. A mixture design methodology is first employed to characterise printed elastomers, generating response surface models (ReSMs) that map material composition to functional properties. Based on user-specified target requirements, a desirability function is then applied for multi-objective optimisation, yielding an optimal operating window of compositions. This enables the fabrication of elastomers with desired properties in a single iteration through monolithic manufacturing. Experimental validation confirms the effectiveness of i-Tac for elastomer customisation and demonstrates its potential for the complete fabrication of VBTSs with tailored performance.

1 | Introduction

Elastomers provide compliance for flexible sensing and inherent safety in physical interaction, which has been widespread used in vision-based tactile sensors (VBTSs) [1]. Among them, silicone is widely employed owing to (1) excellent deformability making it ideal as an interaction medium, protecting devices from damages, and (2) broad tuneability with adjustable elasticity and colour by varying solution mixture ratio; casting temperature, time and pressure; or additional chemical components. In VBTS, external contact induces elastomer deformation under mechanical stimuli [2]. The sensing mechanism subsequently converts these interactions into measurable visual features, such as pixel intensity variations and marker displacements [3], which are captured by the embedded vision system. Consequently, the optical and mechanical properties of VBTS elastomer play a decisive role in above mapping process, with transparency and hardness being the most representative metrics to facilitate tactile sensing. Across different VBTS designs, the required elastomer properties span a broad spectrum, ranging from soft to stiff [4–6] and from optically clear to translucent [7–9]. This diversity necessitates tailoring of elastomer properties to meet the demands of various application scenarios.

However, the conventional mould-casting approach faces limitations in property tailoring of silicone elastomers: (1) it is highly sensitive to manufacturing variables, making it difficult to guarantee reliable elastomer property; and (2) it relies on a forward design paradigm, where production must first be carried out, and only after the real elastomer properties have been evaluated can the manufacturing parameters be adjusted towards the desired target. As illustrated in Figure 1A.a, this trial-and-error optimisation requires repeated prototyping, making the process cumbersome and inefficient. Although the first limitation of mould

This is an open access article under the terms of the Creative Commons Attribution License, which permits use, distribution and reproduction in any medium, provided the original work is properly cited.

© 2026 The Author(s). *Advanced Intelligent Systems* published by Wiley-VCH GmbH.

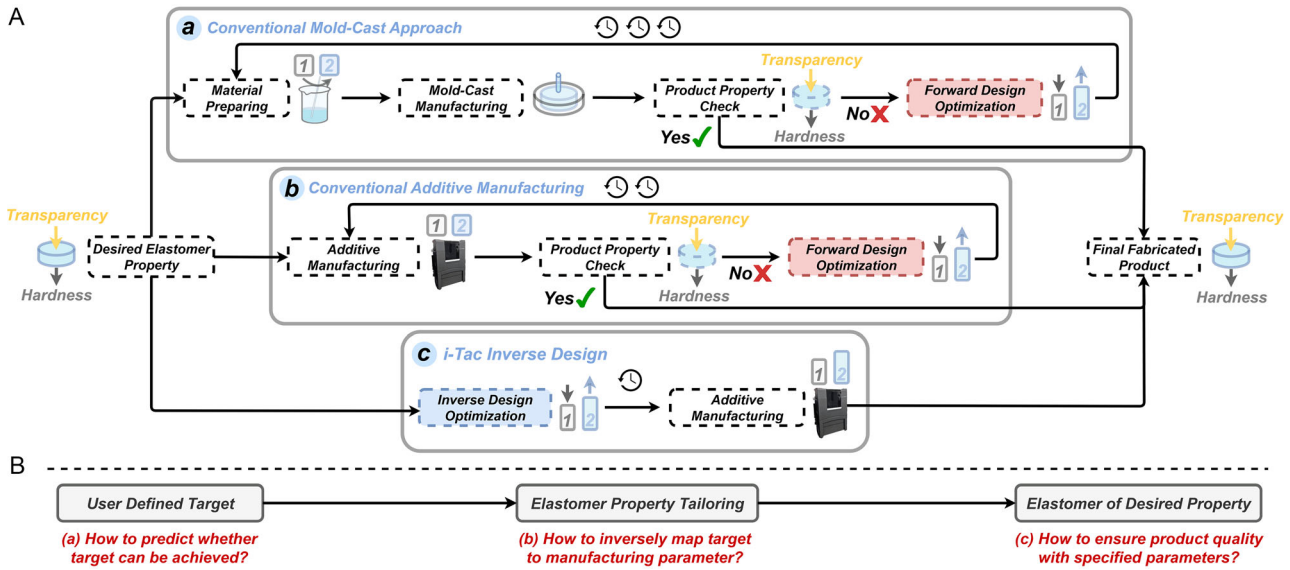


FIGURE 1 | (A) Comparison between forward design and inverse design paradigm in elastomer property tailoring. (a)/(b) Forward design requires prototyping in advance of parameter modification, though additive manufacturing can accelerate fabrication. (c) Inverse design of i-Tac helps additive manufacturing in rapid elastomer tailoring without iteration. (B) Challenges to be addressed in elastomer property tailoring.

casting may be alleviated by enforcing strict production standards, the second is intrinsic to the forward design pipeline and thus represents the principal barrier to efficiency improvement. Although physics-based or semi-empirical models can be employed to pre-calibrate mould-cast elastomers for VBTS [10], this approach requires blending silicone phases with similar curing conditions and therefore offers limited flexibility for simultaneous multi-objective property customisation. Finally, this limitation affects VBTS fabrication not only by prolonging the development cycle but also by introducing performance variability in the finished products. By contrast, an inverse design paradigm, which predicts necessary manufacturing parameters from desired properties, can directly bypass the production in such initial stages. It is therefore essential to establish inverse design–based strategies for tailoring elastomer properties in VBTS applications.

Recently, additive manufacturing has been introduced into VBTS fabrication [2] as a promising alternative that enables faster production, with 3D-printed elastomers being investigated to the same extent as mould-cast samples in tactile sensing [11]. Furthermore, studies such as [3, 12, 13] have explored the fabrication of entire sensor contact modules in a single piece through multi-material additive manufacturing, incorporating all sub-components, including the elastomer. This approach enables the rapid production of structurally complex VBTS designs. However, most of these techniques primarily emphasise flexibility in shaping elastomer geometries—such as structural dimensions or nested configurations within the sensor—while research into tailoring elastomer properties remains limited. Consequently, although current additive manufacturing methods improve prototyping efficiency, the customisation of 3D-printed elastomer properties, such as transparency or hardness, still relies on repeated cycles of production and modification within a forward design pipeline as shown in Figure 1A.b.

To overcome these limitations, we seek to establish a new approach inspired by biological principles. In human tactile sensing [14], the skin functions as the primary medium, whose physiological structure provides valuable insights for elastomer design. In Figure 2A, skin exhibits a multilayered architecture: (1) epidermis forms a thin protective layer of keratinocytes; (2) hypodermis, composed mainly of adipose tissue, connects to deeper muscles and bones; (3) between them lies the dermis, which governs the skin's mechanical behaviour. The dermis is itself a composite of collagen fibres (70%), elastic fibres (4%) and ground substance (20%), interspersed with mechanoreceptors responsible for tactile sensing. Collagen fibres provide high stiffness but limited extensibility, elastic fibres are both highly extensible and elastic, and the fluidic ground substance is soft and viscoelastic. The interplay of these distinct components gives rise to the superior biomechanical properties of human skin, which not only ensures robustness and adaptability under diverse mechanical conditions, but also exemplifies how the integration of materials with complementary properties can achieve functional performance that surpasses any single constituent alone.

Motivated by this biological mixture principle, we propose to achieve tailored elastomer performance for VBTSs by combining 3D print materials with complementary properties. As shown in Figure 2B, three PolyJet printing (PP) materials are introduced: Agilus30 Clear (AC),[1] TissueMatrix (TM),[2] and GelMatrix (GM).[3] Specifically, (1) AC is a rubber-like material with a Shore hardness of 30A and good transparency; (2) TM is much softer, with tissue-like properties and moderate transparency; and (3) GM exhibits gel-like characteristics with high fluidity. Following the principle observed in the dermis of human skin, elastomers printed through AC/TM/GM mixture design can span a wide spectrum of mechanical and optical properties. As illustrated in Figure 2C, monolithic manufacturing [3] maximise this potential through precise digital material assignment rather than manually material preparation, providing an accurate voxel-level mixing to realise above mixture design concept, akin to composite structure in dermis.

Merely introducing an AC/TM/GM mixture design is insufficient for property tailoring in VBTS elastomers, as analysed in Figure 1B; users would still face the intractable task of forward design paradigm between multiple target properties and

26404567, 2026, 8, Downloaded from https://advanced.onlinelibrary.wiley.com/doi/10.1002/aisy.202501200 by Imperial College London, Wiley Online Library on [25/08/2026]. See the Terms and Conditions (https://onlinelibrary.wiley.com/terms-and-conditions) on Wiley Online Library for rules of use; OA articles are governed by the applicable Creative Commons License

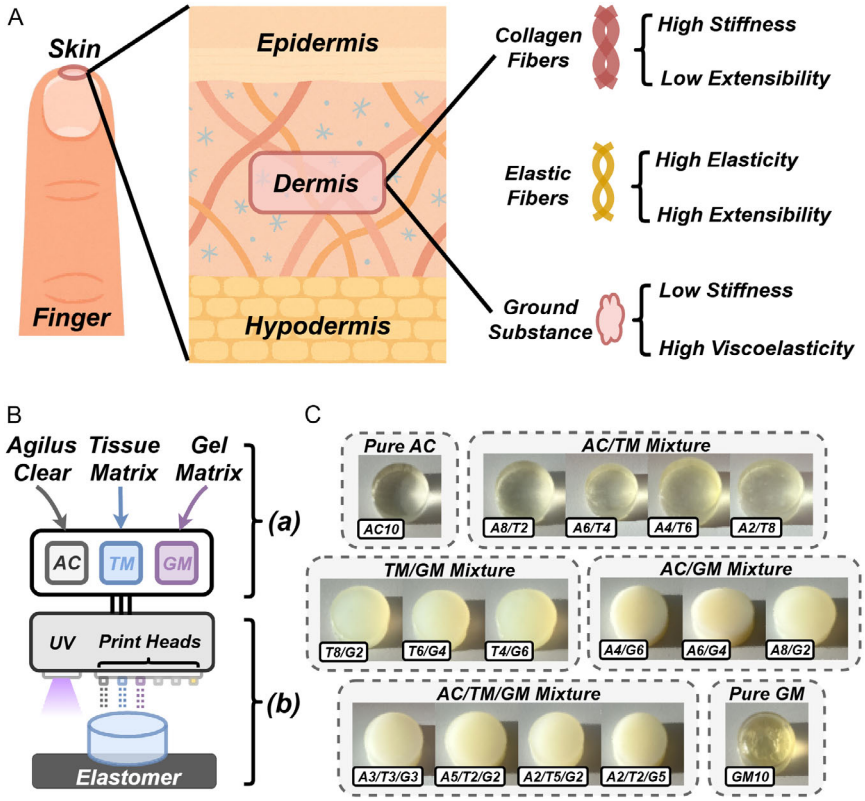


FIGURE 2 | (A) Physiological anatomy of human skin, where dermis layer consists of three distinct tissues. (B) Inverse design of tailoring elastomer property based on (a) AC/TM/GM mixture design and (b) monolithic manufacturing. (C) Wide property range of AC/TM/GM mixture elastomers from clarity to opaque, soft to rigid.

corresponding material compositions. To address this unsolved research question, an inverse design approach is required to enable efficient prediction from desired elastomer properties to optimal mixture configurations, thereby allowing tailored elastomers to be fabricated in a single batch (Figure 1A.c). The main challenge of such prediction, however, lies in the relatively high cost of elastomer property measurement, which constrains large, scale dataset collection. In this regard, statistical approaches, mixture experiment [15], ReSM [16] and desirability function [17], offer suitable solutions, simultaneously satisfying both requirements upon data efficient and interpretable to facilitate elastomer property tailoring.

Then, our proposed inverse design pipeline is illustrated in Figure 3. First, a mixture design space (MDS) is constructed for the AC/TM/GM experiment, and the optical and mechanical properties of the sampled mixtures are modelled using two ReSMs (Figure 3A). Next, given the desired property targets with above ReSMs, a desirability function is employed to perform multi-objective optimisation. Finally, the resulting optimal mixture design is translated into an operational window (Figure 3B), which can be realised through monolithic manufacturing and utilised as inverse-designed elastomer in VBTS (Figure 3C).

The main contributions of this work are as follows:

- We propose an AC/TM/GM mixture design using three complementary printing materials in a multi-material additive manufacturing framework. The design is inspired by the tissue-mixing mechanism of the human finger dermis.

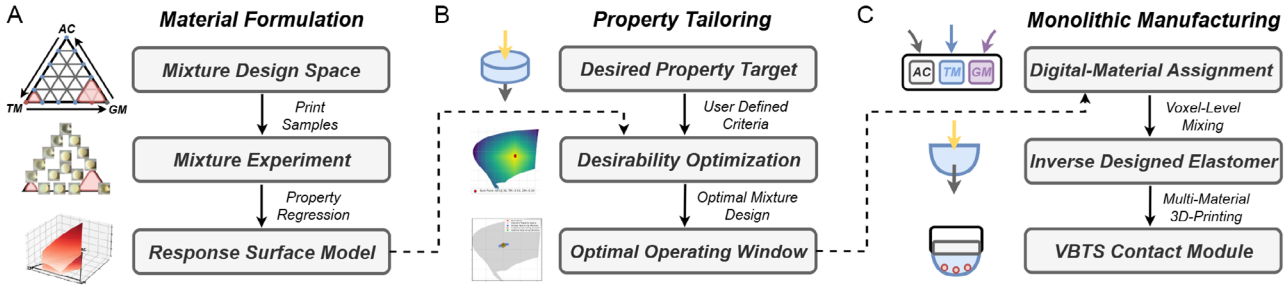


FIGURE 3 | i-Tac inverse design pipeline for elastomer property tailoring of VBTSs. (A) Material formulation, construction of response surface models (ReSMs) mapping AC/TM/GM mixture designs to elastomer properties. (B): Property tailoring, identification of feasible operating windows for 3D printing based on desired property targets using a desirability function. (C) Monolithic manufacturing, realisation of the inverse-designed elastomer in sensor via multi-material printing.

26404567, 2026, 8, Downloaded from https://advanced.onlinelibrary.wiley.com/doi/10.1002/aisy.202501200 by Imperial College London, Wiley Online Library on [25/08/2026]. See the Terms and Conditions (https://onlinelibrary.wiley.com/terms-and-conditions) on Wiley Online Library for rules of use; OA articles are governed by the applicable Creative Commons License

It significantly expands the achievable property range of PolyJet 3D-printed elastomers, covering both optical transparency and mechanical hardness.

- We propose an inverse design pipeline that directly maps target properties to AC/TM/GM mixture design of 3D-printed elastomers. This approach avoids the forward design process and also ensures both interpretability and efficiency of elastomer property tailoring.
- We employ monolithic manufacturing to fabricate real samples with minimal property deviation. The experimental results validate the effectiveness of the proposed mixture design and inverse design pipeline. This strategy narrows the quality gap between 3D-printed sensors and conventionally fabricated VBTS products based on mould-cast silicone and manual assembly.

2 | Related Work

2.1 | Manufacturing Methods for VBTS Elastomer

Existing fabrication approaches for VBTS elastomers fall into two principal categories: mould casting and additive manufacturing [1]. The majority of reported VBTSs employ the mould-casting approach, encompassing both commercially available products and lab-based prototypes [2, 4, 6, 7, 9, 18], as well as those produced by industry [19]. Despite its prevalence, mould casting is constrained by dependence on moulds, laborious processing and variability in product quality [12]. To overcome these limitations, several studies have explored additive manufacturing techniques for VBTS elastomers, such as direct ink writing (DIW) [11] and PP [13]. Compared with DIW, which relies on a single printhead, PP employs arrays of printheads with small nozzles, conferring advantages in multi-material fabrication [3]. Based on that, for the local voxel structure of 3D-printed elastomers, PP employs digital material assignment to achieve precise blending of multiple printing materials, with a ratio accuracy of 1%. Such voxel-level mixing enhances homogeneity and mitigates the fluctuations in product quality that are often observed in mould-cast elastomers, where inaccuracies typically stem from manual material preparation. However, PP is restricted to proprietary PP materials rather than widely used commercial silicones, thereby limiting flexibility in tailoring elastomeric properties. Recently, monolithic manufacturing [3, 13] demonstrates PP in achieving softer elastomers, but has to rely on multi-layer grid structure. Based on this, our work advances monolithic manufacturing in developing homogeneous elastomers via bio-inspired multi-material fusion, thereby achieving a broader range of properties.

2.2 | Inverse Design Methods for Desired Material Property

In materials science, inverse design for achieving target material properties can be categorised into four paradigms [20]: (1) experiment-driven; (2) theory-driven; (3) computation-driven; and (4) artificial intelligence (AI)-driven. Within additive manufacturing, machine learning has emerged as a prominent approach under the AI-driven paradigm, owing to its ability to deliver accurate and instant predictions of printed material properties [21]. Recent studies have explored data-driven inverse design methods to tailor the mechanical behaviour of 3D-printed metamaterials. Ha et al. [22] proposed a rapid inverse design framework that reproduces high-fidelity stress–strain responses using generative models. Chai et al. [23] developed a machine-learning pipeline trained on finite element data to programme snapping metamaterials with pronounced nonlinearities. However, data-driven machine-learning approaches require large datasets and are often less interpretable than explicit models [24]. This limitation makes them impractical for VBTS elastomer design, where data acquisition is expensive and labour-intensive. As an alternative, the statistical principles of mixture experiments [15, 25] enable the optimisation of material properties with relatively few samples, while also providing physical insight through explicit mixture design. For instance, Gao et al. [26] applied mixture experiments to investigate how proportional compositions of hemicellulose, cellulose and lignin affect product distributions during hydrothermal treatment. Similarly, in additive manufacturing, Zhang et al. [27] employed mixture experiments to optimise functional ink formulations for aerosol jet printing, using response surface methodology and desirability functions to balance conductivity and printability. Such an approach is well-suited to VBTS elastomer design, as it facilitates explicit and efficient understanding of critical composition–property relationships.

3 | Methodology

For clarity, the principal symbols, abbreviations, and notations used in the following methodology and experiments are summarised in Table 1.

3.1 | MDS

Based on the concept of mixture experiment [15], our work can be defined as a n component mixture problem ($n = 3$):

$$0 \le L_i \le x_i \le U_i \le 1, i = 1, 2, \ldots, n \tag{1}$$

where L_i and U_i denote the lower and upper bounds of each material component x_i due to printer settings, where $x_1 \in [0, 100\%]$, $x_2 \in [0, 80\%], x_3 \in [0, 60\%]$, also satisfying $\sum_{i=1}^{n} x_i = 1$, with each component percentage restricted to integer values $x_i \in \{0\%, 1\%, 2\%, \ldots, 100\%\}$. In general, the composition space of n components corresponds to an $(n-1)$-dimensional simplex; thereby, MDS of AC/TM/GM reduces to an equilateral triangle (x_1, x_2, x_3), represented as a ternary diagram in Figure 4A.

3.2 | Mixture Experiment

3.2.1 | Selected Samples

From MDS, a total of 19 mixtures can be obtained through uniform sampling. Among these, c1 corresponds to the centroid mixture, c2–c4 represent three-component mixtures, while the remainder are binary mixtures. Owing to lower and upper bounds of each material, t1, t5 and g2 are excluded as forbidden mixtures, whereas g1 is isolated for GM optical testing due to its distinctive fluidity. Consequently, 15 samples (a1–a5, t2–t4, g1,

2640567, 2026, 8, Downloaded from https://advanced.onlinelibrary.wiley.com/doi/10.1002/aisy.202501200 by Imperial College London, Wiley Online Library on [25/08/2026]. See the Terms and Conditions (https://onlinelibrary.wiley.com/terms-and-conditions) on Wiley Online Library for rules of use; OA articles are governed by the applicable Creative Commons License

TABLE 1 | Summary of terms used in this paper.

Term	Definition
AC	Agilus30 Clear
TM	Tissue matrix
GM	Gel matrix
x_1	AC component (%)
x_2	TM component (%)
x_3	GM component (%)
(x_1, x_2, x_3)	Mixture design space (MDS)
$Y(x)$	Response surface model (ReSM)
Y_1	ReSM of transparency (%)
Y_2	ReSM of hardness (Shore 00)
Y_1^*, Y_2^*	Optimised ReSM after ANOVA
$x(Y_1, Y_2)$	Feasible property space (FPS)
FPS (AC)	$x_1(Y_1, Y_2)$
FPS (TM)	$x_2(Y_1, Y_2)$
FPS (GM)	$x_3(Y_1, Y_2)$
NTB	Nominal-The-Better desirability criteria
LTB	Larger-The-Better desirability criteria
STB	Smaller-The-Better desirability criteria
T_{Y1}, T_{Y2}	Desired target of transparency/hardness
w_1, w_2	Weight for transparency/hardness
$d(Y)$	Desirability function to reach T_Y
$D(d(Y)\dots)$	Overall desirability function
$(\hat{x}_1, \hat{x}_2, \hat{x}_3)$	Optimal mixture design
$(\hat{Y}_1, \hat{Y}_2)$	ReSM prediction of $(\hat{x}_1, \hat{x}_2, \hat{x}_3)$
$W_{\Delta x}$	Design operating window $(\pm \Delta x\%)$
$W_{\Delta Y}$	Property operating window $(-\Delta Y\%)$
W_{optimal}	Optimal operating window $\{(\hat{x}_1, \hat{x}_2, \hat{x}_3)_0, \dots, (\hat{x}_1, \hat{x}_2, \hat{x}_3)_i\}$
R_{Y1}, R_{Y2}	Real transparency/harness of elastomer
Error1	Error between T_Y and $\hat{Y}$
Error2	Error between $\hat{Y}$ and measured R_Y

g3–g5, c1, c2–c4) are selected for following mixture experiment, with full details provided in Table 2 and illustrated in Figure 4B.

3.2.2 | Optical Property Experiment

To quantitatively analyse the optical transparency of the elastomer, light transmission T as a function of wavelength λ is introduced, defined as the ratio of input to output light intensities:

$$T(\lambda) = \frac{I_{\text{out}}(\lambda)}{I_{\text{in}}(\lambda)} \tag{2}$$

Based on the 15 mixture design samples, a total of 90 cylindrical specimens were fabricated, each with elastomer thicknesses $d_{\text{thick}} = 3, 6, 9$ mm and a diameter of 10 mm, where a 1 mm surface layer of VeroClear was added upon to ensure structural rigidity. All specimens were subsequently placed in a microplate and tested using a spectrometer with a scanning range of $\lambda \in [200, 1000]$ nm, covering the ultraviolet (200–400 nm), visible (400–700 nm) and infrared (700–1000 nm) regions. In addition, multi-layer grid (SUP) [3, 13], VeroClear (VC) and pure air (None) were included as baselines. As an illustrative case, the measured transmission $T(\lambda)$ at $d_{\text{thick}} = 3$ mm is shown in Figure 5A, demonstrating that the light transmittance of the elastomers generally increases with wavelength, while exhibiting marked variations across different mixture designs. Since $T(\lambda)$ is too complex to be a concise indicator, therefore, T_{mix} is defined for each mixture design as its light transmission at a particular wavelength λ for a given elastomer thickness d_{thick}. As most VBTSs are designed to operate with visible light sources, the optical properties within the 400–700 nm range are the most representative for VBTS elastomers. Thereby, $\lambda = 700$ nm is selected, as it provides the highest transmission of each mixture design within the visible range (Figure 5B). On this basis, the relationship between T_{mix} and d_{thick} can be examined using the Beer–Lambert law [28], which relates absorbance A, path length d, extinction coefficient ε and concentration c of an absorbing substance:

$$A = -\log_{10}(T) = \varepsilon\, c\, d \tag{3}$$

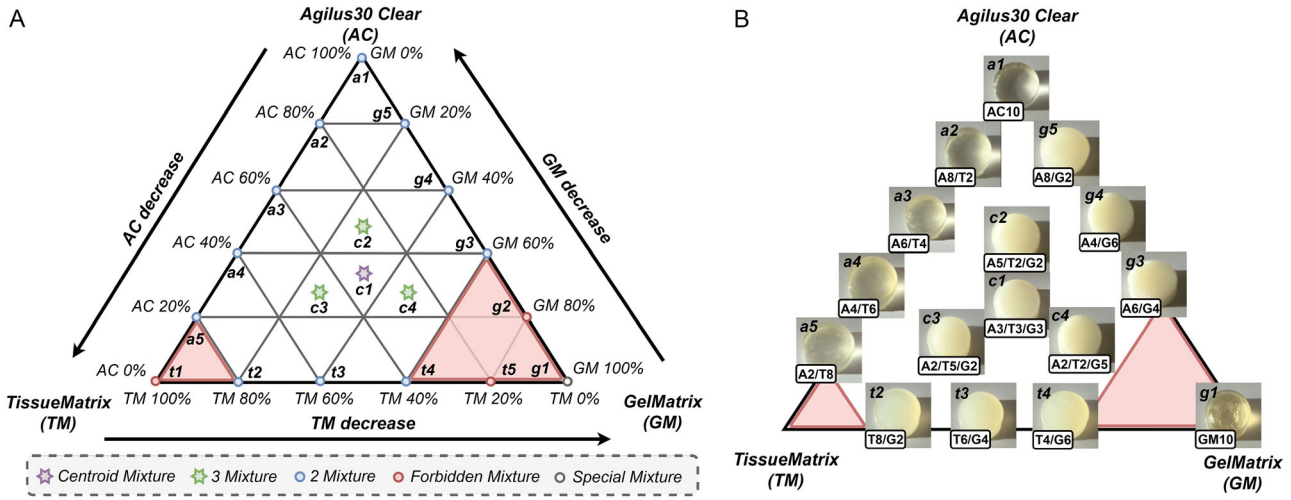


FIGURE 4 | (A) MDS of AC/TM/GM component, with centroid mixture (c1), 3-mixture (c2–c4), 2-mixture (a1–a5, t2–t4, g3–g5), forbidden mixture (t1, t5, g2) and special mixture (g1). (B) Fifteen samples (a1–a5, t2–t4, g1, g3–g5, c1–c4) are fabricated for mixture experiment.

26404567, 2026, 8, Downloaded from https://advanced.onlinelibrary.wiley.com/doi/10.1002/aisy.202501200 by Imperial College London, Wiley Online Library on [25/08/2026]. See the Terms and Conditions (https://onlinelibrary.wiley.com/terms-and-conditions) on Wiley Online Library for rules of use; OA articles are governed by the applicable Creative Commons License

TABLE 2 | Selected samples for mixture experiment.

Type	Sample	Mixture design	x_1	x_2	x_3x_3
2-mixture	**a1**	AC10	100%	0	0
	a2	AC8/TM2	80%	20%	0
	a3	AC6/TM4	60%	40%	0
	a4	AC4/TM6	40%	60%	0
	a5	AC2/TM8	20%	80%	0
	t2	TM8/GM2	0	80%	20%
	t3	TM6/GM4	0	60%	40%
	t4	TM4/GM6	0	40%	60%
	g3	AC4/GM6	40%	0	60%
	g4	AC6/GM4	60%	0	40%
	g5	AC8/GM2	80%	0	20%
3-mixture	**c1**	A3/T3/G3	33%	34%	34%
	c2	A5/T2/G2	50%	25%	25%
	c3	A2/T5/G2	25%	50%	25%
	c4	A2/T2/G5	25%	25%	50%

By setting the path length d equal to d_{thick} and introducing a bias transmission T_{bias} measured from pure-air baseline, the absorbance of mixture design and opacity density per unit thickness can be mathematically expressed as:

$$A_{\text{mix}} = -\log_{10}(T_{\text{mix}} + (1 - T_{\text{bias}})) = c_{\text{opacity}}\, d_{\text{thick}} \tag{4}$$

$$c_{\text{opacity}} = \frac{\log_{10}\left(T_{\text{mix}} + (1 - T_{\text{bias}})\right)}{d_{\text{thick}}} \tag{5}$$

Finally, c_{opacity} characterises the effective 'opacity density per unit thickness' of the mixture design samples. As shown in Figure 5C, c_{opacity} at $d_{\text{thick}} = 3$ mm exhibits a more uniform distribution compared with the clustered convergence observed at 6 mm and 9 mm, indicating improved differentiation of the mixture design characteristics.

3.2.3 | Mechanical Property Experiment

Similarly, Shore 00 hardness is employed to characterise the mechanical properties of the mixture designs. In contrast to the optical specimens, larger specimens with a diameter of 30 mm and a thickness of 12 mm were fabricated for the mechanical experiments. For each sample, five hardness measurements were uniformly collected from the surface using a Shore 00 durometer, yielding a total of 75 data points across 15 mixture designs. The results are presented in Figure 5D, which reflect a linear relationship between elastomer hardness and the mixture compositions.

3.2.4 | Mixture Experiment Result

As shown in Figure 6A, transmission $T_{\text{mix}} = T(700nm)$ is recorded as the optical transparency data of mixture design sample ($d_{\text{thick}} =$ 3 mm), representing its most clarity within visible light range. Furthermore, using such a single representative wavelength is appropriate for VBTS, where illumination prioritises overall transmittance rather than detailed spectral shaping. From Figure 5A, the mixtures exhibit near-linear, monotonic spectra with a peak transmittance around 700 nm. Therefore, the single-wavelength metric preserves the relative ordering of candidate materials for VBTS selection. As shown in Table 3, it can be further corrected as unbiased transparency by T_{bias} of pure-air measurement. From Figure 6B, Shore 00 is selected as the mechanical property metric since AC/TM/GM mixtures substantially extend hardness beyond beyond Shore A measurement range. Based on these two criteria, example results of mixture experiments are illustrated in Figure 6C and detailed in Table 3. With respect to optical properties, all AC/TM mixtures exhibit a high transparency of 70–80%, whereas TM/GM mixtures show significantly reduced transmission, ranging from 30% down to 15%. Other designs, such as AC/GM and three-component mixtures, rapidly become opaque, with transmission falling below 10% or approaching zero. Regarding mechanical hardness, values decrease linearly from Shore 00-85 to 00-40 as AC fraction is reduced from 100% to 20%, a trend also observed for AC/GM mixtures. The addition of TM or GM further softens the samples compared with AC-based designs, with TM/GM mixtures reaching as low as Shore 00-30 or even 00-20. Collectively, these results demonstrate that AC/TM/GM mixtures can expand the accessible range of both optical and mechanical properties of printed elastomers, highlighting their strong potential for inverse design in property tailoring.

3.3 | ReSM

3.3.1 | Quadratic Regression Formulation

Based on the experimental data summarised in Table 3, a ReSM is employed to perform regression fitting for transparency and hardness, thereby extending the limited sample measurements from MDS to the full property prediction surface. In particular, the cubic Scheffé model [29] is adopted to characterise the relationships between transparency/hardness (Y_1/Y_2) and the volume fractions of the mixture design components (x_1, x_2, x_3):

$$Y_{\text{m}} = \sum_{i=1}^{n} \beta_{\text{i}}^{m} x_{\text{i}} + \sum_{1 \le i < j}^{n} \beta_{ij}^{m} x_{\text{i}} x_{\text{j}} + \sum_{1 \le i < j < k}^{n} \beta_{ijk}^{m} x_{\text{i}} x_{\text{j}} x_{k}, \tag{6}$$

where $n = 3$ corresponds to AC/TM/GM components, $m \in [1, 2]$ represents the transparency/hardness properties and β denotes the regression coefficients. The terms x_{i}, $x_{\text{i}}x_{\text{j}}$ and $x_{\text{i}}x_{\text{j}}x_{\text{k}}$ represent the main effects (AC, TM, GM), the two-way interactions (AC/TM, AC/GM, TM/GM) and the three-way interaction (AC/TM/GM), respectively. The regression coefficients β are estimated using the ordinary least squares (OLS) method:

$$\hat{\beta} = \arg\min_{\beta} \|y - X\beta\|^2 = (X^{\top}X)^{-1}X^{\top}y \tag{7}$$

Based on the fitted parameters $\hat{\boldsymbol{\beta}}$, the regression models for transparency (Y_1) and hardness (Y_2) are obtained as follows:

$$\begin{aligned} Y_1 = {} & 82.5\,x_1 + 71.9\,x_2 + 110.6\,x_3 + 27.1\,x_1x_2 - 362.1\,x_1x_3 \\ & - 233.2\,x_2x_3 - 167.6\,x_1x_2x_3 \end{aligned} \tag{8}$$

$$\begin{aligned} Y_2 = {} & 83.3\,x_1 + 28.1\,x_2 - 9.2\,x_3 + 23.9\,x_1x_2 + 68.7\,x_1x_3 \\ & + 49.6\,x_2x_3 + 57.1\,x_1x_2x_3 \end{aligned} \tag{9}$$

26404567, 2026, 8, Downloaded from https://advanced.onlinelibrary.wiley.com/doi/10.1002/aisy.202501200 by Imperial College London, Wiley Online Library on [25/09/2026]. See the Terms and Conditions (https://onlinelibrary.wiley.com/terms-and-conditions) on Wiley Online Library for rules of use; OA articles are governed by the applicable Creative Commons License

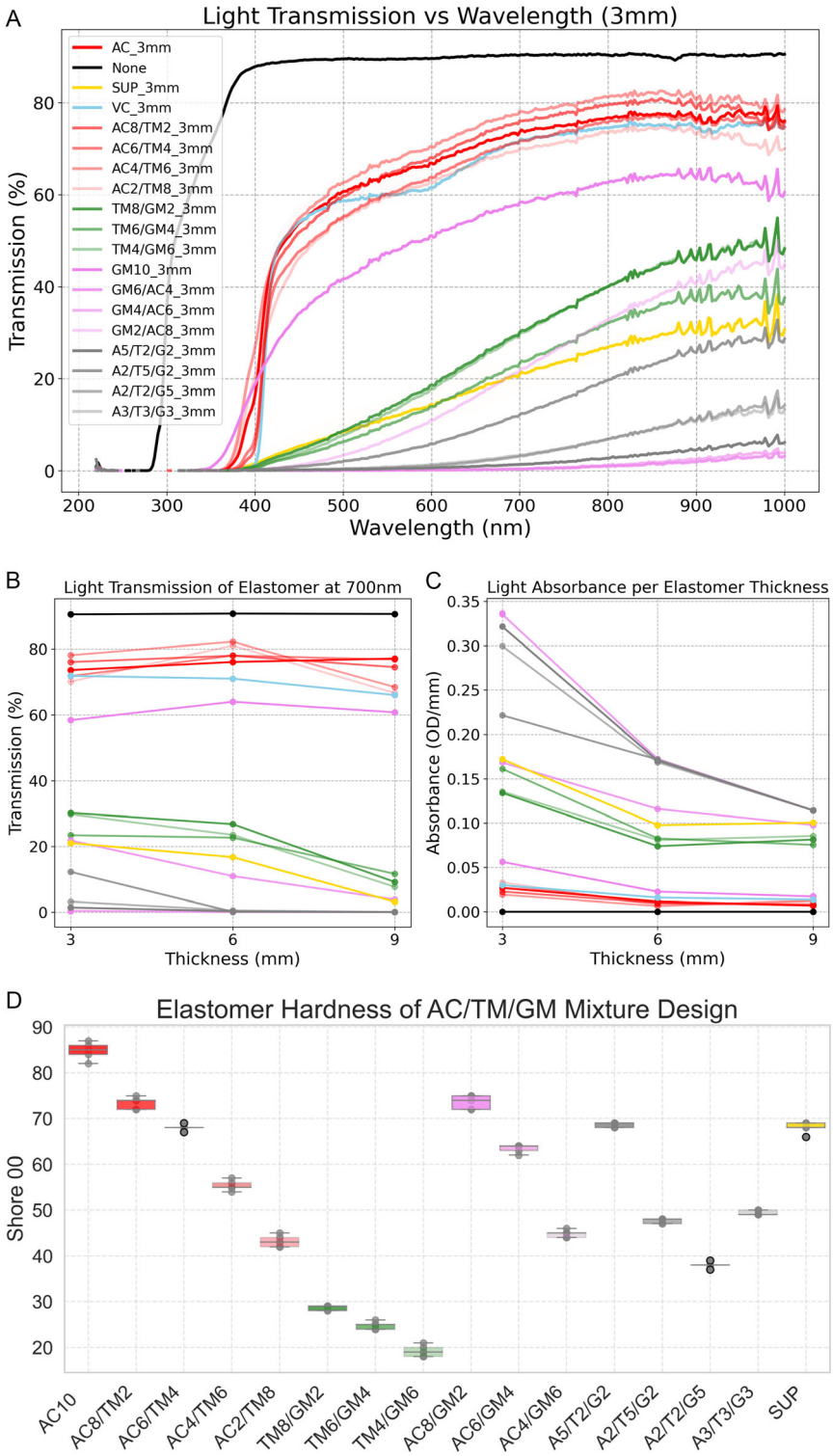


FIGURE 5 | (A) Light transmission per wavelength of mixture design samples with 3 mm thickness. (B) Light transmission at 700 nm with different sample thickness. (C) Opacity density per unit thickness. (D) Mechanical hardness of mixture design samples.

3.3.2 | ANOVA for Model Optimisation

Analysis of variance (ANOVA) is applied to refine the initial regression models Y_1 and Y_2 by removing independent factors with negligible influence on the dependent variables, as summarised in Table 4. For Y_1, the p-values of x_{12} and x_{123} are significantly higher than those of the other terms, indicating that the AC/TM and three-way interactions have limited impact on optical transparency and can thus be omitted. Similarly, in the case of Y_2, the terms x_3 and x_{123} yield the largest p-values, suggesting that GM and the three-way interaction contribute less to mechanical hardness. Two optimised regression models, Y_1^* and Y_2^*, are therefore proposed, with their performance evaluated in Table 4. For Y_1^*, model simplification by excluding x_{12} and x_{123} results in lower RMSE (greater predictive accuracy), higher R^2 or

26404567, 2026, 8, Downloaded from https://advanced.onlinelibrary.wiley.com/doi/10.1002/aisy.202501200 by Imperial College London, Wiley Online Library on [25/08/2026]. See the Terms and Conditions (https://onlinelibrary.wiley.com/terms-and-conditions) on Wiley Online Library for rules of use; OA articles are governed by the applicable Creative Commons License

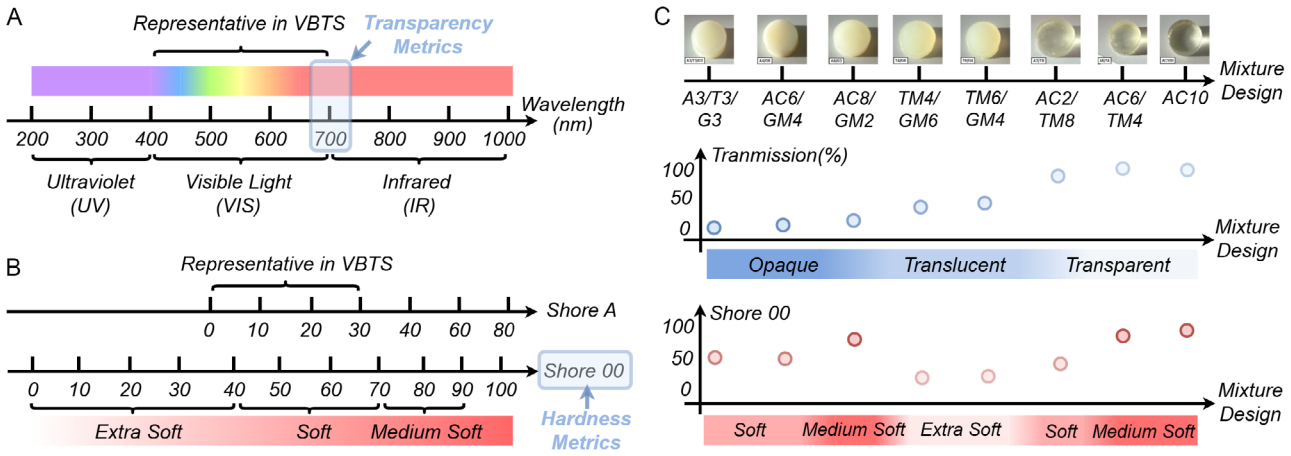


FIGURE 6 | (A) Transparency metrics in optical mixture experiment. (B) Hardness metrics in mechanical mixture experiment. (C) Experiment results in terms of optical transparency and Shore 00 hardness, where selected mixture design samples both show wide property ranges.

TABLE 3 | Mixture experiment results of transparency/hardness.

Mixture design	Unbiased transparency	Hardness (Shore 00)
AC10	83.06%	84.8
AC8/TM2	85.25%	73.4
AC6/TM4	81.23%	68.0
AC4/TM6	87.59%	55.4
AC2/TM8	79.56%	43.2
TM8/GM2	39.61%	28.6
TM6/GM4	32.83%	24.8
TM4/GM6	39.19%	19.2
AC4/GM6	9.78%	44.8
AC6/GM4	9.85%	63.4
AC8/GM2	31.24%	73.6
A3/T3/G3	42.73%	49.4
A5/T2/G2	10.84%	68.6
A2/T5/G2	21.66%	47.6
A2/T2/G5	12.62%	38.0
GM10	67.79%	Gel-like
VC	81.3%	Rigid
SUP	30.46%	68.0
Pure air	100.0%	-

adjusted R^2 (indicating improved variable selection) and lower AIC/BIC (more concise formulation). In contrast, Y_2^* achieves greater simplicity (lower AIC/BIC) but suffers from reduced prediction accuracy (higher RMSE) when omitting x_3 and x_{123}. Since GM plays a critical role, x_3 is reintroduced, leading to improved regression precision compared with the initial Y_2. The final optimised models are thus denoted as $Y_1{}^*$ and $Y_2{}^*$:

$$Y_1^* = 85.1x_1 + 78.8x_2 + 124.2x_3 - 399.1x_1x_3 - 281.6x_2x_3 \quad (10)$$

$$Y_2^* = 82.5x_1 + 26.2x_2 - 13.7x_3 + 31.6x_1x_2 + 81.0x_1x_3 + 65.1x_2x_3 \quad (11)$$

3.3.3 | ReSM Analysis

Based on ANOVA optimisation results, two corresponding ReSMs, $Y_1 = Y_1^*(x_1, x_2, x_3)$ and $Y_2 = Y_2^*(x_1, x_2, x_3)$, are respectively constructed to enable an intuitive material property formulation from mixture designs $x_1/x_2/x_3$ to elastomer properties Y_1/Y_2, with their 2D contour maps illustrated in Figure 7. For the transparency ReSM (Figure 7A), its response surface exhibits a non-monotonic variation: higher proportions of AC (x_1) and TM (x_2) generally lead to greater transparency (Y_1) of the printed elastomer. Moreover, when the GM (x_3) content remains below 10%, Y_1 consistently exceeds 55%. In contrast, the hardness ReSM (Figure 7B) presents a more homogeneous distribution. The vertex occurs at pure AC ($x_1 = 100\%$), and hardness gradually decreases along the axis extending towards TM/GM (x_2/x_3). The softest region of Y_2 lies along the TM/GM edge, indicating an inverse relationship between hardness Y_2 and the AC fraction (x_1).

3.3.4 | FPS

To lay the foundation for subsequent inverse design tasks, three FPSs are investigated, $x_1(Y_1, Y_2)$, $x_2(Y_1, Y_2)$ and $x_3(Y_1, Y_2)$, which reversely maps from Y_1/Y_2 to $x_1/x_2/x_3$, as illustrated in Figure 8. It characterises the overall property distribution of mixture designs, whose outline represents the inverse design boundary. Furthermore, the UV-cured nature and partially overlapping property ranges of AC, TM and GM promote smooth property variation with mixing ratio, supported by the near-linear hardness trends observed at the feasible space boundaries (Figure 5D). In addition, the convex combination formulation of the mixture design physically bounds the achievable properties within the envelope defined by the pure constituents. This constraint reduces the risk of unexpected discontinuities. A larger FPS area indicates broader elastomer properties achievable through mixture design, thereby providing greater inverse design generalisability. As shown in Figure 8, the overall FPS exhibits an irregular property envelope with a parallelogram-shaped region on the right, indicating that the range of Y_1 between 40% and 80% and Y_2 between Shore 00-40 and 00-80 can be largely attained through appropriate combinations of $x_1/x_2/x_3$. In contrast, the left region of the FPS forms a triangular cone, reflecting the difficulty of achieving either ultra-hard or ultra-soft properties in opaque mixtures. Moreover, the lower portion of the FPS

26404567, 2026, 8, Downloaded from https://advanced.onlinelibrary.wiley.com/doi/10.1002/aisy.202501200 by Imperial College London, Wiley Online Library on [25/08/2026]. See the Terms and Conditions (https://onlinelibrary.wiley.com/terms-and-conditions) on Wiley Online Library for rules of use; OA articles are governed by the applicable Creative Commons License

TABLE 4 | ANOVA optimisation of response surface model.

	Y_1		Y_1^*		Y_2		$Y_2^*(-x_3)$		$Y_2^*(+x_3)$	
	F	***P***	***F***	***P***	***F***	***P***	***F***	***P***	***F***	***P***
x_1	73.992	<0.0001	150.149	<0.0001	1018.021	<0.0001	1199.306	<0.0001	1288.709	<0.0001
x_2	15.207	0.0045	73.575	<0.0001	31.445	<0.0001	44.940	<0.0001	43.334	0.0001
x_3	6.452	0.0347	14.487	0.0034	0.603	0.4597	—	—	2.085	0.183
x_{12}	0.194	0.6712	—	—	2.029	0.1921	5.651	0.0388	6.983	0.0268
x_{13}	13.059	0.0068	34.690	0.0002	6.357	0.0357	37.341	0.0001	16.697	0.0027
x_{23}	3.836	0.0859	15.179	0.0030	2.347	0.1641	9.994	0.0101	8.531	0.0170
x_{123}	0.294	0.6021	—	—	0.461	0.5159	—	—	—	—
RMSE ↓	10.605		9.664		2.886		2.946		2.798	
R^2↑	0.979		0.978		0.999		0.998		0.998	
Adj. R^2 ↑	0.960		0.967		0.997		0.997		0.997	
AIC ↓	117.980		114.540		78.935		78.902		77.777	
BIC ↓	122.936		118.080		83.892		82.442		82.026	

Note: '$Y_2^*(-x_3)$' represents Y_2^* without x_3; '$Y_2^*(+x_3)$' indicates Y_2^* with reintroduced x_3.

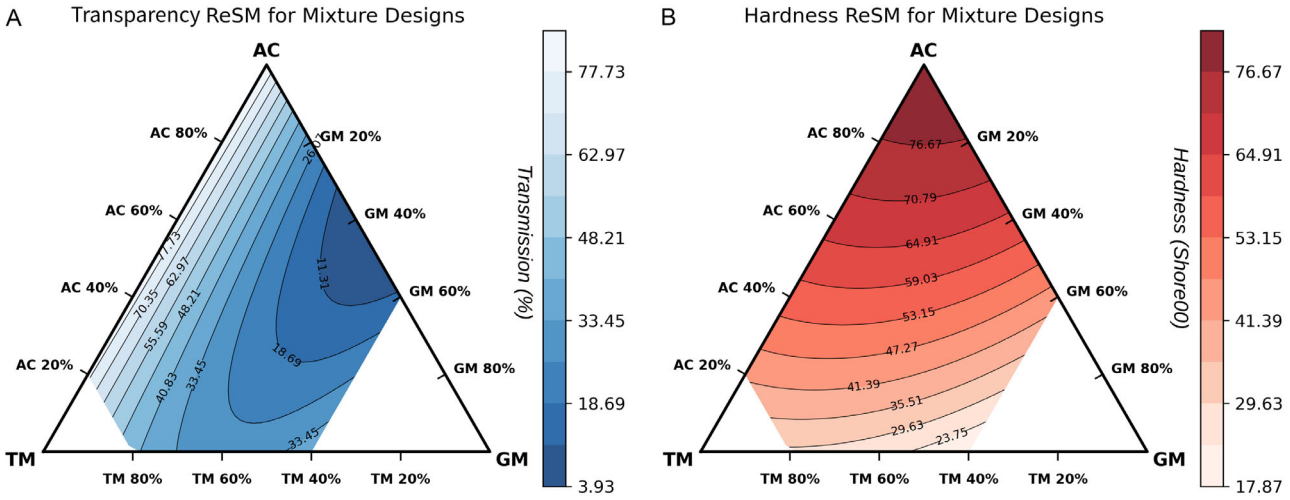


FIGURE 7 | (A) Transparency ReSM for mixture designs. (B) Hardness ReSM for mixture designs.

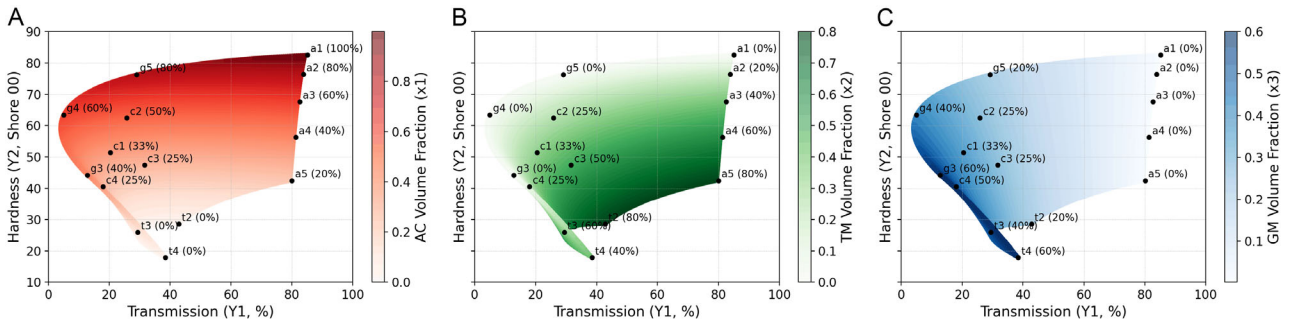


FIGURE 8 | Feasible property space (FPS). (A) FPS(AC), $x_1(Y_1, Y_2)$, effects more in higher hardness area. (B) FPS(TM), $x_2(Y_1, Y_2)$, effects more in lower hardness area. (C) FPS(GM), $x_3(Y_1, Y_2)$, effects more in lower clarity and ultra-soft area.

presents an irregular triangular shape, suggesting that the generalisability of Y_1 is more constrained when Y_2 falls below Shore 00-40. Further insights into FPS can be obtained by analysing the roles of x_1, x_2 and x_3 individually. For FPS(AC) (Figure 8A), its primary influence is observed in the upper half of the FPS, where higher x_1 values correspond to higher Y_2. Notably, the full Y_1 range (5-80%) can be covered when x_1 is between 40% and 50%. By contrast, FPS(TM) (Figure 8B) mainly governs the lower FPS region, where larger x_2 values lead to softer Y_2. Additionally, the gradients of both x_1 and x_2 align

26404567, 2026, 8, Downloaded from https://advanced.onlinelibrary.wiley.com/doi/10.1002/aisy.202501200 by Imperial College London, Wiley Online Library on [25/08/2026]. See the Terms and Conditions (https://onlinelibrary.wiley.com/terms-and-conditions) on Wiley Online Library for rules of use; OA articles are governed by the applicable Creative Commons License

nearly parallel to Y_1, indicating that their variations contribute less significantly to transparency. Finally, FPS(GM) (Figure 8C) dominates the left side of the FPS, where x_3 remains below 15% whenever $Y_1 > 40\%$, confirming that GM strongly induces opacity.

3.4 | Inverse Design for Property Tailoring

The inverse design method for tailoring elastomer property is illustrated in Figure 9, which will be introduced as follow:

3.4.1 | Desirability Function

Given the desired property of both (T_{Y_1}, T_{Y_2}), desirability function approach [17] is employed to address multi-objective optimisation to locate optimal mixture design of ($\hat{x}_1, \hat{x}_2, \hat{x}_3$). It evaluates both responses through a common scale of desirability, where three criteria are typically used: (1) Nominal-The-Better (NTB), (2) Larger-The-Better (LTB) and (3) Smaller-The-Better (STB).

$$d_{\mathrm{NTB}}(Y_{\mathrm{i}}) = \begin{cases} 0, & Y_{\mathrm{i}} < L_{Y_{\mathrm{i}}} \text{ or } Y_{\mathrm{i}} > U_{Y_{\mathrm{i}}}, \\ \left(\frac{Y_{\mathrm{i}} - L_{Y_i}}{T_{Y_i} - L_{Y_i}}\right)^r, & L_{Y_i} \le Y_{\mathrm{i}} \le T_{Y_i}, \\ \left(\frac{U_{Y_i} - Y_{\mathrm{i}}}{U_{Y_i} - T_{Y_i}}\right)^r, & T_{Y_i} < Y_i \le U_{Y_i}, \end{cases} \tag{12}$$

$$d_{\mathrm{LTB}}(Y_{\mathrm{i}}) = \begin{cases} 0, & Y_i < L_{Y_i}, \\ \left(\frac{Y_i - L_{Y_i}}{U_{Y_i} - L_{Y_i}}\right)^r, & L_{Y_i} \le Y_i \le U_{Y_i}, \\ 1, & Y_i > U_{Y_i}, \end{cases} \tag{13}$$

$$d_{\mathrm{STB}}(Y_{\mathrm{i}}) = \begin{cases} 0, & Y_i > U_{Y_i}, \\ \left(\frac{Y_i - U_{Y_i}}{L_{Y_i} - U_{Y_i}}\right)^r, & L_{Y_i} \le Y_i \le U_{Y_i}, \\ 1, & Y_i < L_{Y_i}. \end{cases} \tag{14}$$

For NTB, the objective is to bring the response value Y_i as close as possible to a predefined target T_{Y_i}, with desirability $d_{NTB}(Y_i)$ decreasing as the response deviates from this target. In contrast, LTB and STB impose one-sided preferences: LTB aims to maximise the response value Y_i (towards an upper bound U_{Y_i}), while STB aims to minimise it (towards a lower bound L_{Y_i}). To facilitate intuitive inverse design, a comprehensive guideline for selecting desirability criteria is summarised in Table 5. In total, nine criteria guidance are provided to accommodate diverse design objectives, covering a broad spectrum of elastomer property requirements. Specifically, when users aim for a well-defined specification on both transparency and hardness, the NTB/NTB (Id-1) is recommended, as it identifies a crossover point that simultaneously satisfies both targets. If the design goal is to maximise one property while constraining the other to a fixed indicator, then NTB/LTB or NTB/STB (Id-2/3/4/7) are suitable

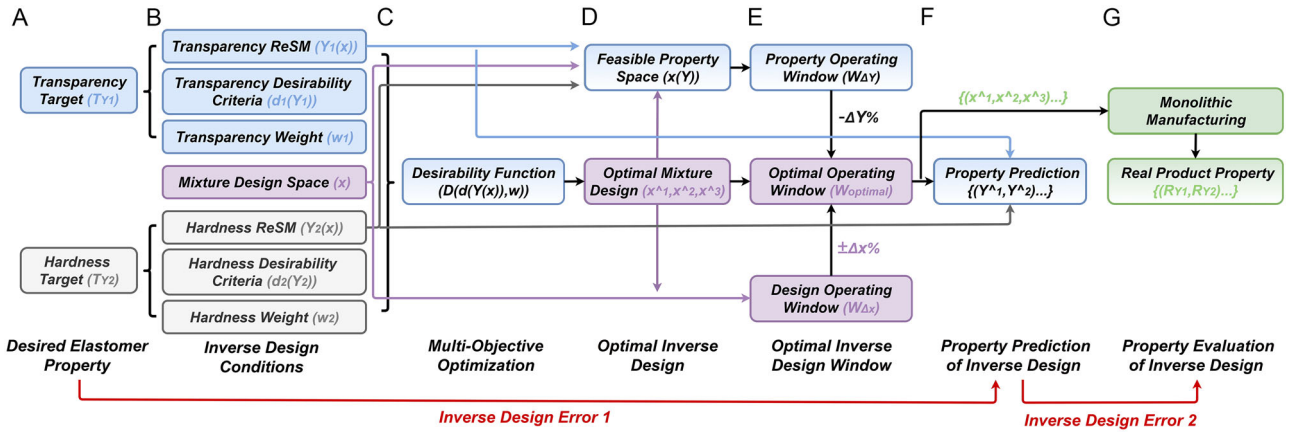


FIGURE 9 | Inverse design methodology for tailoring elastomer property. (A) Desired elastomer property. (B) Required material formulations and user preference. (C) Multi-objective optimisation between different property targets. (D) Optimal inverse design. (E) Optimal inverse design window for elastomer fabrication. (F) Property prediction of inverse-designed elastomer. (G) Real evaluated property of elastomer product.

TABLE 5 | Desirability criteria guideline for inverse design for tailoring elastomer property.

Guidance Id	Y_1criteria	Y_2criteria	Tailoring elastomer property	Inverse design application
Id-1	NTB	NTB	Specific elastomer transparency and hardness	Targeted elastomer customisation
Id-2	NTB	LTB	Hardest elastomer based on a specific transparency	Hardness optimisation
Id-3	NTB	STB	Softest elastomer based on a specific transparency	Hardness optimisation
Id-4	LTB	NTB	Clearest elastomer based on a specific hardness	Transparency optimisation
Id-5	LTB	LTB	Clearest and hardest elastomer	Ultra-rigid clear elastomer
Id-6	LTB	STB	Clearest and softest elastomer	Ultra-soft clear elastomer
Id-7	STB	NTB	Most opaque elastomer based on a specific hardness	Transparency optimisation
Id-8	STB	LTB	Most opaque and hardest elastomer	Ultra-rigid opaque elastomer
Id-9	STB	STB	Most opaque and softest elastomer	Ultra-soft opaque elastomer

26404567, 2026, 8, Downloaded from https://advanced.onlinelibrary.wiley.com/doi/10.1002/aisy.202501200 by Imperial College London, Wiley Online Library on [25/08/2026]. See the Terms and Conditions (https://onlinelibrary.wiley.com/terms-and-conditions) on Wiley Online Library for rules of use; OA articles are governed by the applicable Creative Commons License

choices. Finally, LTB/STB (Id-5/6/8/9) are most appropriate for users seeking the property boundaries of mixture design. Once the desirability functions (d_1, d_2) are selected as (T_{Y_1}, T_{Y_2}), respectively, the overall desirability function D [17] can be formulated as:

$$D(T_{Y_1}, T_{Y_2}) = D(d_1(Y_1), d_2(Y_2)) = \left(\prod_{i=1}^{2} d_i(Y_i)^{w_i} \right)^{1/\sum w_i} \quad (15)$$

where $w_i \in [w_1, w_2]$ denotes user-defined weights assigned to criterion of (d_1,d_2), allowing preference adjustment between (T_{Y_1}, T_{Y_2}) in cases of objective optimisation conflict. In this way, independent targets T_{Y_i} are unified under a single formulation D, parameterised by user-defined criteria d_i and weights w_i. Then, optimisation task becomes finding the maximum value of D, which yields the optimal composition $(\hat{x}_1, \hat{x}_2, \hat{x}_3)$ [17]:

$$\begin{aligned} \hat{x}_1, \hat{x}_2, \hat{x}_3 &= \arg \max_{x_1, x_2, x_3} D(T_{Y_1}, T_{Y_2}) \\ &= \arg \max \left(\textstyle\prod_{i=1}^{2} d_i(Y_i(x_1, x_2, x_3))^{w_i} \right)^{\frac{1}{\sum w_i}} \\ \text{s.t. } & \textstyle\sum x_i = 1, \sum w_i = 1 \\ & 0 \le x_1 \le 1, 0 \le x_2 \le 0.8, 0 \le x_3 \le 0.6. \end{aligned} \quad (16)$$

3.4.2 | Optimal Operating Window

Although the desirability function enables multi-objective optimisation, its single optimal solution $(\hat{x}_1, \hat{x}_2, \hat{x}_3)$ is generally obtained as floating-point percentages. Such fractional compositions cannot be directly implemented on a printer for monolithic fabrication. To enhance practical feasibility, it is therefore necessary to explore a set of near-optimal solutions with integer-valued compositions. For this purpose, we introduce the optimal operating window approach.

As illustrated in Figure 10A, the first step is to locate the optimal solution $(\hat{x}_1, \hat{x}_2, \hat{x}_3)$ in the MDS. Around this point, floating thresholds ($\pm \Delta x\%$) are applied to each component, thereby generating a design operating window $W_{\Delta x}$. In parallel, within the FPS (Figure 10B), the corresponding ReSM predictions $(\hat{Y}_1, \hat{Y}_2)$ of $(\hat{x}_1, \hat{x}_2, \hat{x}_3)$ are taken as benchmarks, where a tolerance margin ($-\Delta Y\%$) is then applied along its descending gradient of the desirability function ΔD, yielding a property operating window $W_{\Delta Y}$. Finally, the intersection of $W_{\Delta x}$ and $W_{\Delta Y}$ defines optimal operating window $W_{optimal}$ in FPS. As shown in Figure 10C, $W_{optimal}$ contains i set of integer-percentage designs$\{(\hat{x}_1, \hat{x}_2, \hat{x}_3)_0, \ldots, (\hat{x}_1, \hat{x}_2, \hat{x}_3)_i\}$, which can be then employed for monolithic manufacturing.

3.4.3 | Inverse Design Error Analysis

To evaluate the proposed method in Figure 9, we introduce the concept of the inverse design error, which is composed of two components:

1. Error1: defined as the discrepancy between the desired elastomer property (T_{Y_1}, T_{Y_2}) and the corresponding property prediction from ReSM, $\{(\hat{Y}_1, \hat{Y}_2)_0, \ldots, (\hat{Y}_1, \hat{Y}_2)_i\}$, based on optimal operating window $\{(\hat{x}_1, \hat{x}_2, \hat{x}_3)_0, \ldots, (\hat{x}_1, \hat{x}_2, \hat{x}_3)_i\}$.
2. Error2: defined as the deviation between the ReSM-predicted properties, $\{(\hat{Y}_1, \hat{Y}_2)_0, \ldots, (\hat{Y}_1, \hat{Y}_2)_i\}$, and the experimentally evaluated properties of the 3D-printed elastomer, $\{(R_{Y_1}, R_{Y_2})_0, \ldots, (R_{Y_1}, R_{Y_2})_i\}$.

Specifically, Error1 assesses the outcome of the multi-objective optimisation based on the desirability function when a property tailoring target is specified (Figure 3B). This enables an evaluation of whether the chosen desirability criteria and weight parameters lead to an optimal mixture design consistent with user-defined preferences. By contrast, Error2 serves to evaluate the generalisation capability of the ReSM in material formulation (Figure 3A). In this case, for a given mixture design, the greater the predictive accuracy of the ReSM, the closer the realised elastomer properties will be to the predicted values, thereby reducing Error2.

4 | Experiment

As illustrated in Figure 3, the proposed i-Tac pipeline provides three principal advantages: (1) it introduces an AC/TM/GM mixture design strategy to expand the feasible material property space of 3D-printed elastomers; (2) it establishes an inverse design framework for systematically tailoring the properties of mixture-designed elastomers; and (3) the PolyJet-based monolithic manufacturing approach enables direct fabrication of complete VBTS contact modules, thereby simplifying the production workflow and improving manufacturing efficiency. In this

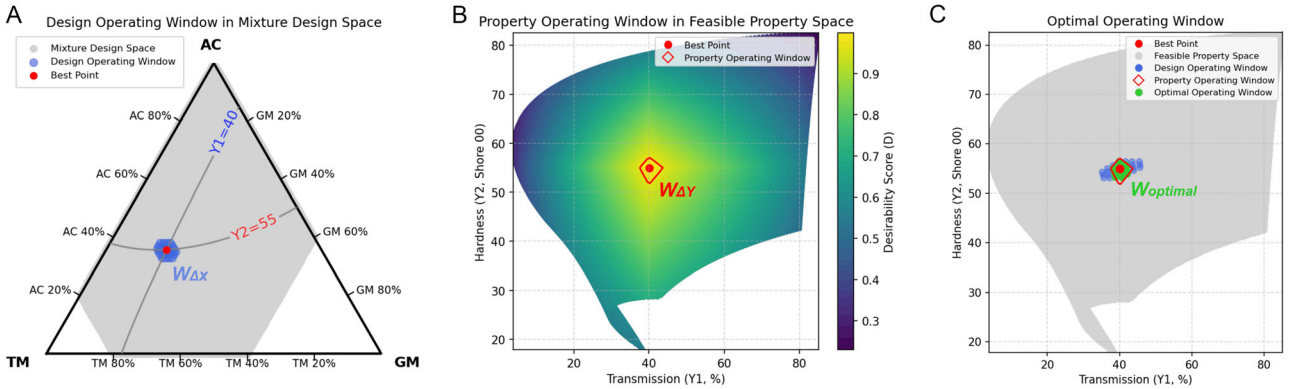


FIGURE 10 | (A) Design operating window $W_{\Delta x}$ with user-defined $\pm \Delta x\%$. (B) Property operating window $W_{\Delta Y}$ with user-defined $-\Delta Y\%$. (C) Optimal operating window W_{optimal}, defines i set of integer-percentage designs $\{(x_1, x_2, x_3)_0, \ldots, (x_1, x_2, x_3)_i\}$ for subsequent printing.

26404567, 2026, 8, Downloaded from https://advanced.onlinelibrary.wiley.com/doi/10.1002/aisy.202501200 by Imperial College London, Wiley Online Library on [25/08/2026]. See the Terms and Conditions (https://onlinelibrary.wiley.com/terms-and-conditions) on Wiley Online Library for rules of use; OA articles are governed by the applicable Creative Commons License

section, a series of experiments are conducted to validate the aforementioned advantages.

4.1 | Material Property Evaluation of Mixture Designs

4.1.1 | Material Properties for Tactile Sensing

As shown in Figure 11A, multiple material properties of VBTS elastomers critically influence tactile sensing performance: (1) hardness characterises the resistance of an elastomer to surface indentation; (2) Poisson's ratio quantifies the volumetric change during deformation; (3) the elastic modulus reflects the resistance to bulk deformation under tensile or compressive loading; and (4) hysteresis describes the recovery behaviour when the external load is removed. To systematically analyse these factors, we establish the evaluation pipeline illustrated in Figure 11B. This framework enables comparative assessment among 3D-printed mixture designs and in comparison with mould-cast silicone elastomers.

For benchmarking purposes, five commercial silicone products widely adopted in VBTS research [1] are included, covering a broad spectrum from transparent to opaque and from ultra-soft to relatively stiff materials: (1) Ecoflex 00-31 and 00-45:[4] ultra-soft, platinum-cured silicones with excellent optical clarity, curing at room temperature within approximately 4 h, with Shore 00-31 and 00-45 hardness, respectively; (2) DragonSkin 20 and 30:[5] opaque, platinum-cured silicone rubbers with high tensile strength, curing at room temperature within 4–16 h, with Shore 20A and 30A hardness; (3) SORTA-Clear 40:[6] a near-transparent, platinum-cured silicone rubber, curing at room temperature within approximately 16 h, with Shore 40A hardness.

The results of the tensile and compression evaluations are presented in Figure 12A,B, with detailed experimental procedures provided in Appendix A. For tensile behaviour, commercial silicones typically exhibit elastic moduli in the range of 50–350 kPa. In contrast, conventional PolyJet elastomers such as AC and SUP show comparatively high stiffness (450 kPa and 270 kPa, respectively). By employing the proposed mixture design, the effective modulus range of 3D-printed elastomers is expanded to approximately 100–250 kPa. Meanwhile, tensile hysteresis is substantially reduced from 0.3–0.6 to 0.05–0.3, approaching the 0.05–0.1 range commonly observed in commercial silicones.

A similar trend is observed under compression. The mixture designs extend the compressive modulus range from the baseline values of AC (150 kPa) and SUP (65 kPa) to nearly 10–100 kPa, while reducing compression hysteresis from 0.5 and 0.3 to 0.1–0.5. These values move closer to the typical ranges of commercial silicones (compressive modulus, 30–220 kPa; hysteresis, 0.1–0.3).

Overall, compared to typical PolyJet-printed elastomers, the experimental results indicate that AC/TM/GM mixture designs provide (i) improved force sensitivity due to reduced modulus, (ii) enhanced flexibility in sensor design enabled by an expanded modulus range and (iii) faster dynamic response associated with lower hysteresis. Collectively, these improvements help narrow the performance gap between PolyJet-printed elastomers and conventional mould-cast silicones. A comprehensive summary of the evaluated material properties is provided in Table 6. In addition to hardness, the measured Poisson's ratio of the mixture-designed elastomers fluctuates around 0.4. Considering the measurement uncertainty of the DIC system and the commonly assumed value of 0.49 for nearly incompressible commercial silicones, the volumetric compressibility of the proposed mixtures is expected to be comparable to that of conventional silicone materials.

4.1.2 | Material Property Correlation

Based on the above investigation, both 3D-printed mixture designs and mould-cast silicone have considerable overlap in material property. Therefore, another investigation is introduced to analyse the correlation between their material properties.

From Figure 12 C.a, hardness, elastic modulus and compressive modulus of all materials can be fitted to a response surface. If exclude outliers, the most material points converge into a narrow

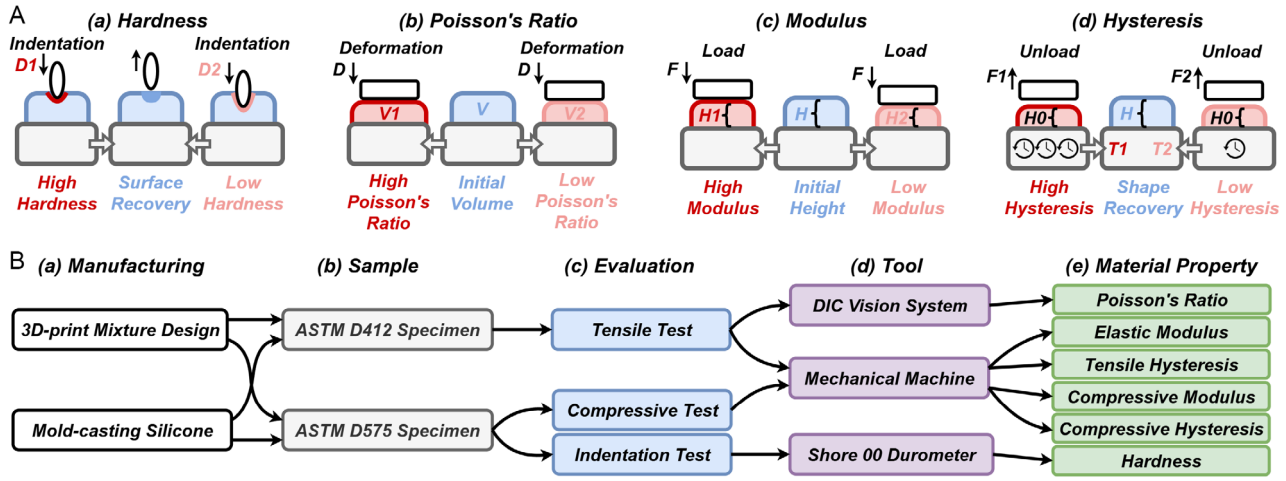


FIGURE 11 | (A) Influence of elastomer material properties on tactile sensing. (a) Hardness reflects the resistance of the sensor surface to indentation; (b) Poisson's ratio characterises the volumetric change of the elastomer during deformation; (c) modulus indicates the resistance to bulk deformation under external loading; (d) hysteresis quantifies the recovery rate of the sensor after load removal. (B) Investigation pipeline for elastomer material characterisation. (a) i-Tac mixture design and mould-casting methods; (b) sample preparation following ASTM standards; (c) three mechanical evaluation tests; (d) instrumentation for experimental data acquisition; (e) six material properties considered in the analysis.

26404567, 2026, 8, Downloaded from https://advanced.onlinelibrary.wiley.com/doi/10.1002/aisy.202501200 by Imperial College London, Wiley Online Library on [25/08/2026]. See the Terms and Conditions (https://onlinelibrary.wiley.com/terms-and-conditions) on Wiley Online Library for rules of use; OA articles are governed by the applicable Creative Commons License

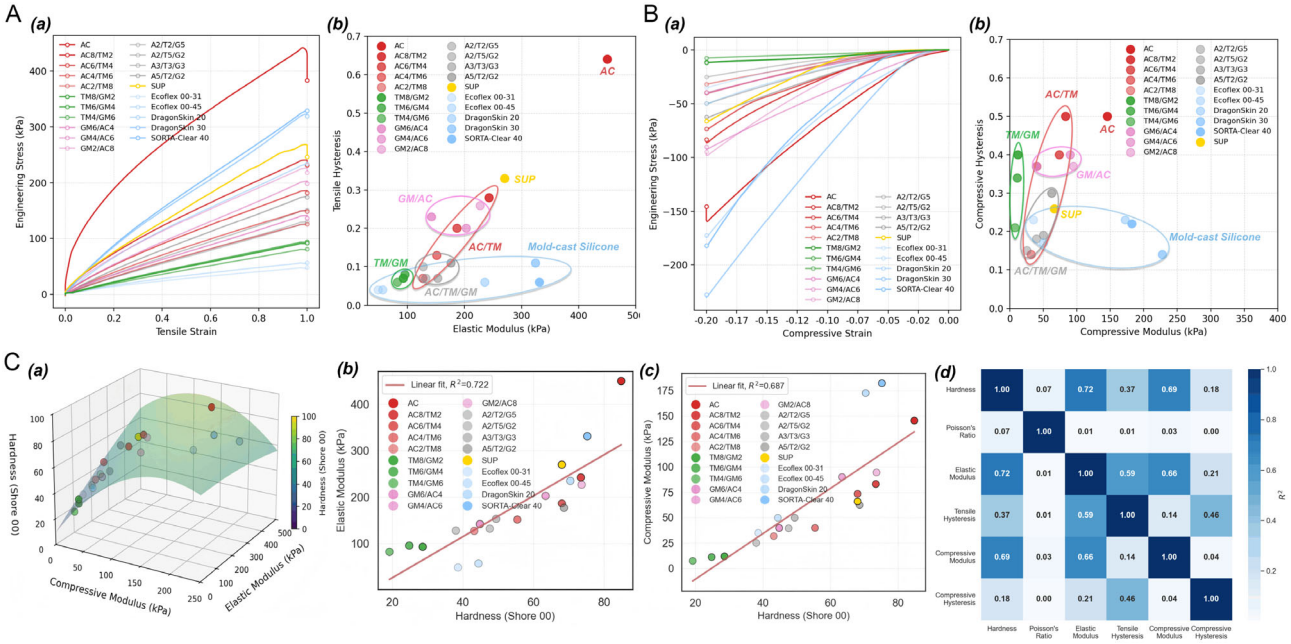


FIGURE 12 | (A) Uniaxial tensile testing results. (a) Representative stress–strain curve under uniaxial tension; (b) relationship between tensile hysteresis and elastic modulus. (B) Uniaxial compression testing results. (a) Representative stress–strain curve under uniaxial compression; (b) relationship between compressive hysteresis and compressive modulus. (C) Correlations among elastomer material properties. (a) Response surface fitting of hardness, elastic modulus and compressive modulus; (b,c) linear relationships between elastomer hardness and elastic/compressive modulus; (d) cross-property correlations.

TABLE 6 | Material property comparison between 3D-printed mixture design and mould-cast elastomers.

Mixture design	Hardness (Shore 00)	Poisson's ratio	Elastic modulus (kPa)	Tensile hysteresis	Compressive modulus (kPa)	Compressive hysteresis
AC10	84.8	0.42	449.87	0.64	145.45	0.50
AC8/TM2	73.4	0.38	242.68	0.28	83.15	0.50
AC6/TM4	68.0	0.41	186.60	0.20	73.55	0.40
AC4/TM6	55.4	0.42	151.35	0.13	39.77	0.37
AC2/TM8	43.2	0.41	127.02	0.07	31.75	0.14
TM8/GM2	28.6	0.40	92.80	0.07	11.83	0.40
TM6/GM4	24.8	0.45	95.39	0.08	11.13	0.34
TM4/GM6	19.2	0.45	82.03	0.06	7.39	0.21
AC4/GM6	44.8	0.42	141.68	0.23	39.70	0.37
AC6/GM4	63.4	0.36	202.99	0.20	90.09	0.40
AC8/GM2	73.6	0.38	227.04	0.26	94.56	0.37
A3/T3/G3	49.4	0.43	152.88	0.07	49.71	0.19
A5/T2/G2	68.6	0.37	176.83	0.11	62.32	0.30
A2/T5/G2	47.6	0.39	131.95	0.07	39.43	0.18
A2/T2/G5	38.0	0.45	127.68	0.10	24.98	0.15
SUP	68.0	0.43	270.08	0.33	65.95	0.26
Ecoflex 00-31	38.6	0.35	48.53	0.04	34.89	0.23
Ecoflex 00-45	44.4	0.33	56.99	0.04	49.67	0.17
DragonSkin 20	70.4	0.41	235.40	0.06	172.45	0.23
DragonSkin 30	75.0	0.38	324.30	0.11	227.77	0.14
SORTA-Clear 40	75.2	0.40	331.25	0.06	182.16	0.22

26404567, 2026, 8, Downloaded from https://advanced.onlinelibrary.wiley.com/doi/10.1002/aisy.202501200 by Imperial College London, Wiley Online Library on [25/08/2026]. See the Terms and Conditions (https://onlinelibrary.wiley.com/terms-and-conditions) on Wiley Online Library for rules of use; OA articles are governed by the applicable Creative Commons License

inclined plane, which implies existing correlations. Linear regression model is used to analyse this trend, which indicates a positive correlation between hardness and both modulus (Figure 12 C.b/c). More comprehensively, all correlations across material properties are analysed with R^2 results shown in Figure 12 C.d. In summary, hardness and modulus are closely connected with R^2 locates around 0.7, while Poisson's ratio is not significantly correlated with others. Similar to modulus, a correlation also exists between tensile and compressive hysteresis with a R^2 of around 0.5.

The above analyses are essential because, in many cases, a complete characterisation of material properties cannot be achieved due to experimental constraints or application-specific conditions. In such situations, rational correlations can be employed to predict unknown properties, for example, by estimating the elastic modulus from the more readily measured elastomer hardness. The observed correlations among material properties across mixture designs further demonstrate the generalisability of the i-Tac framework in inverse design tasks. Specifically, if i-Tac can tailor elastomer hardness, it can be readily extended to achieve comparable performance in targeting elastic or compressive modulus, thereby broadening the applicability of the framework.

4.2 | Inverse Design Performance on Property Tailoring

4.2.1 | Tailoring Target from Desirability Criteria Guideline

To assess the effectiveness of the proposed desirability function approach for inverse design, nine groups of desired elastomer properties (T_{Y_1}, T_{Y_2}) were defined according to desirability criteria guideline in Table 5. The corresponding evaluation results are summarised in Figure 13 and Table 7.

For Id-1, Id-2 and Id-3, the T_{Y_1} is consistently set to 55% under the NTB criterion. Following multi-objective optimisation using the desirability function, although T_{Y_2} criterion varies to LTB or STB, their predicted values $\hat{Y}_1$ based on optimal mixture design $(\hat{x}_1, \hat{x}_2, \hat{x}_3)$ remain close to the desired 55%. Similarly, Id-4, Id-5 and Id-6 all adopt the LTB criterion for T_{Y_1}, while Id-7, Id-8 and Id-9 adopt the STB criterion. Their corresponding predictions $\hat{Y}_1$ successfully reproduce the expected trends, ranging correctly from higher values (79.18%–83.91%) to lower values (17.5%–29.83%) in terms of selected T_{Y_1} of LTB and STB, respectively.

Furthermore, in Id-1 through Id-7, the weights w_1/w_2 are set to 0.5:0.5, thereby ensuring no objective bias in the desirability optimisation. For instance, Id-1 specifies both targets T_{Y_1} and T_{Y_2} as 55, yielding predicted values of $\hat{Y}_1 = 55.3\%$ and $\hat{Y}_2 = 55.08\%$. In contrast, Id-8 and Id-9 share the same T_{Y_1} but adopt different weighting schemes. Specifically, Id-8, with $w_1/w_2 = 3:7$, is more strongly biased towards T_{Y_2} (hardness), whereas Id-9, with $w_1/w_2 = 6:4$, places greater emphasis on T_{Y_1} (transparency). It further indicates that the optimal inverse design $(\hat{x}_1, \hat{x}_2, \hat{x}_3)$ for Id-8 is $(74, 0, 26)$, involving only x_1 and x_3 while excluding x_2, since the AC/GM mixture can simultaneously provide moderate opacity and enhanced hardness. By comparison, the optimal mixture design for Id-9 is $(0, 54, 46)$, which relies exclusively on x_2 and x_3 rather than x_1, in order to achieve optimal opacity and moderate softness. This is consistent with the fact that AC-based mixtures inherently increase both transparency and rigidity found during material formulation (Figure 7).

Such results demonstrate that the proposed desirability function method is capable of fidelity realising diverse inverse design tasks defined by criteria guidelines, while also allowing user preferences to be flexibly incorporated into above multi-objective optimisation through adjustable weight coefficients.

TABLE 7 | Inverse design of desirability criteria guideline.

Id	T_{Y_1}	T_{Y_2}	w_1	w_2	$\hat{x}_1$	$\hat{x}_2$	$\hat{x}_3$	$\hat{Y}_1$	$\hat{Y}_2$
Id-1	55	55	0.5	0.5	36	54	10	55.30	55.08
Id-2	55	LTB	0.5	0.5	91	0	9	54.98	80.41
Id-3	55	STB	0.5	0.5	9	80	11	55.04	35.43
Id-4	LTB	60	0.5	0.5	46	54	0	80.73	60.01
Id-5	LTB	LTB	0.5	0.5	100	0	0	83.91	82.49
Id-6	LTB	STB	0.5	0.5	20	80	0	79.18	42.33
Id-7	STB	60	0.5	0.5	33	7	60	17.5	40.15
Id-8	STB	LTB	0.3	0.7	74	0	26	17.98	72.91
Id-9	STB	STB	0.6	0.4	0	54	46	29.83	23.89

4.2.2 | Tailoring Target from Real Silicone Samples

As shown in Figure 14A, two casting moulds, Mold-A and Mold-B, were fabricated with dimensions identical to the specimens used in mixture experiments. Subsequently, all silicones were prepared and cast at room temperature in accordance with the manufacturers' guidelines, followed by property testing. The resulting measurements were then used as T_{Y_1} and T_{Y_2}, as summarised in Table 8. In this process, most desirability criteria were specified as NTB, with all desirability weights w_1/w_2 set to 0.5:0.5. In addition, ultra-soft Ecoflex 00-31 was assigned the STB criterion for T_{Y_2}

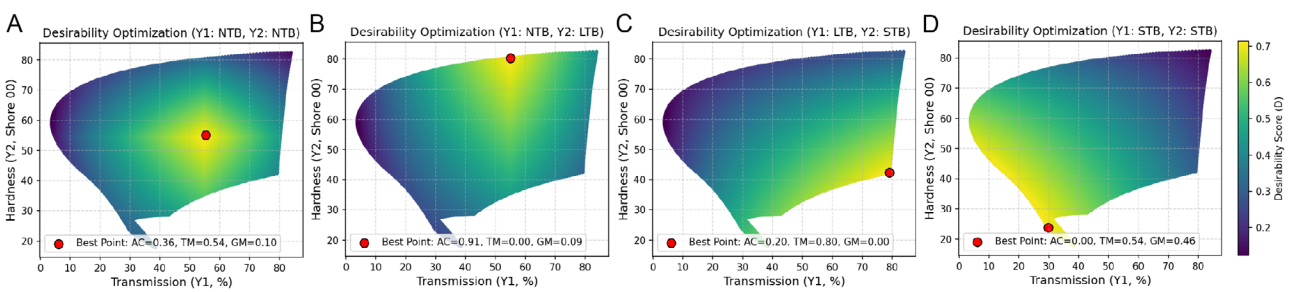


FIGURE 13 | Case study of desirability optimisation in terms of criteria guideline. (A) NTB/NTB; (B) NTB/LTB; (C) LTB/STB; (D) STB/STB.

26404567, 2026, 8, Downloaded from https://advanced.onlinelibrary.wiley.com/doi/10.1002/aisy.202501200 by Imperial College London, Wiley Online Library on [25/08/2026]. See the Terms and Conditions (https://onlinelibrary.wiley.com/terms-and-conditions) on Wiley Online Library for rules of use; OA articles are governed by the applicable Creative Commons License

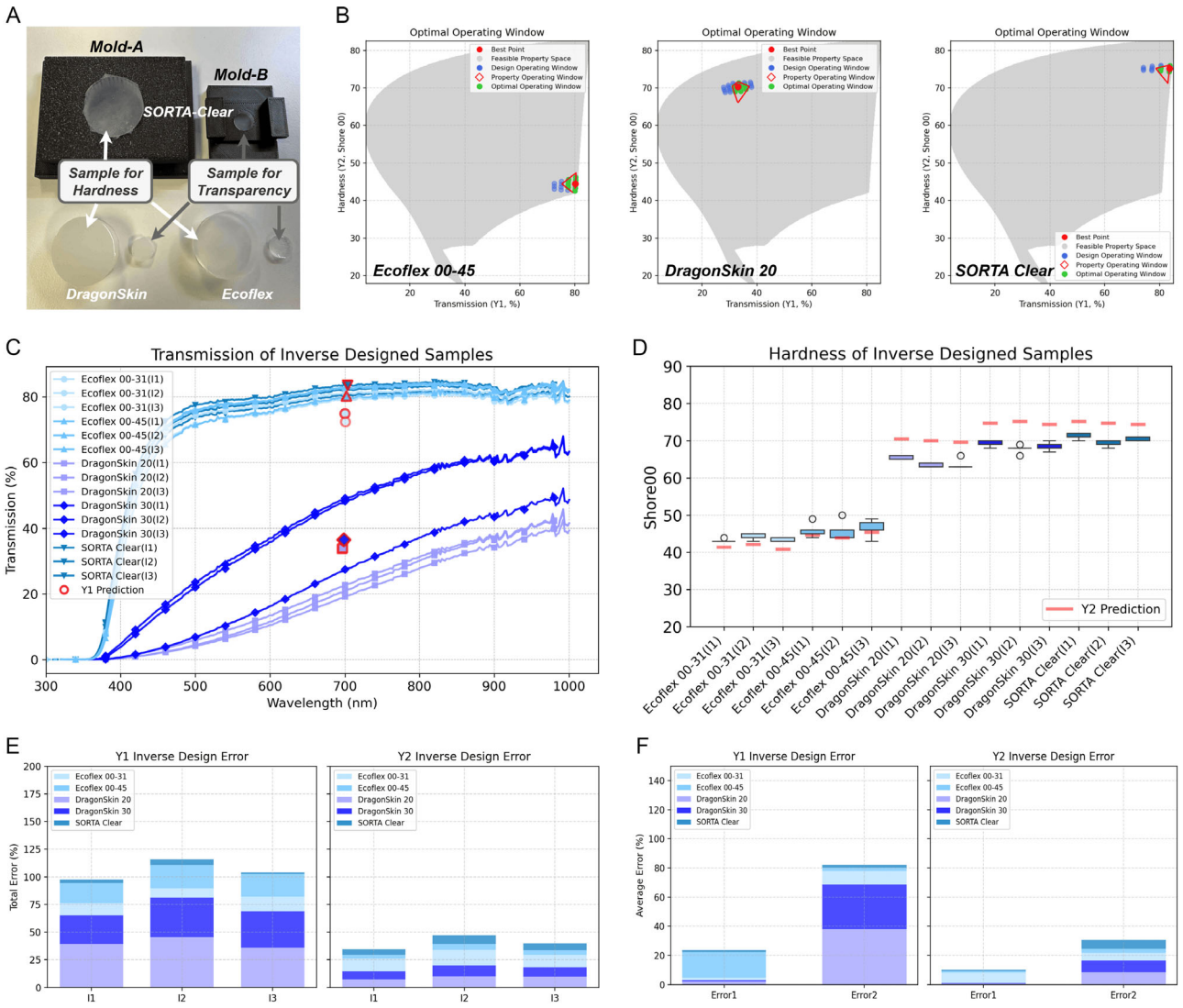


FIGURE 14 | (A) Mould-casting silicone (Ecoflex, DragonSkin, SORTA Clear). (B) Optimal operating window tailoring from real silicone. (C) Real transparency R_{Y_1} and predicted $\hat{Y}_1$ (red edges) of inverse design samples. (D) Real hardness R_{Y_2} and predicted $\hat{Y}_2$ (red lines) of inverse design samples. (E) Accumulated inverse design error compared between $I_1/I_2/I_3$. (F) Average inverse design error compared between Error1/Error2.

in order to minimise hardness, whereas T_{Y_1} of ultra-clear Ecoflex 00-45 and SORTA Clear were assigned the LTB criterion to maximise transparency. The optimal operating window $\{(\hat{x}_1,\hat{x}_2,\hat{x}_3)_0, \ldots,(\hat{x}_1,\hat{x}_2,\hat{x}_3)_i\}$ was then determined by applying tolerance thresholds of $\Delta x\%$ and $\Delta Y\%$, both set at 3%, as illustrated in Figure 14B. Among these, three inverse designs with the highest desirability values were selected and denoted as I_1, I_2 and I_3, with their corresponding mixture designs summarised in Table 8. Finally, based on the above inverse designs, 15 groups of 3D-printed specimens were fabricated through monolithic manufacturing, each consisting of two optical samples and one mechanical sample (45 specimens in total). Their property evaluation results are presented in Figure 14C,D.

In Figure 14C, the predicted elastomer transparency, $\hat{Y}_1$, are highlighted with red edges. At $\lambda = 700$ nm, the experimentally measured R_{Y_1} values for the real specimens of Ecoflex and SORTA Clear inverse designs closely match their predictions, both falling within the range of 75%–80%. For the DragonSkin inverse designs, the R_{Y_1} values of real samples lie between 20% and 45%, covering the predicted range of approximately 35%–40%. In Figure 14D, the predicted elastomer hardness, $\hat{Y}_2$, is indicated by red lines. The 3D-printed elastomers of Ecoflex inverse designs exhibit very low hardness, with measured R_{Y_2} values ranging from Shore 00-40 to 00-50, in close agreement with their $\hat{Y}_2$ predictions. By contrast, the DragonSkin and SORTA Clear inverse designs show a marked increase in hardness towards Shore 00-60 and 00-70, although most of their measured hardness R_{Y_2} are slightly (around 5 units) lower than $\hat{Y}_2$ predictions. These results indicate that the proposed inverse design method achieves a close alignment between predictions and real measurements, particularly for clear or softer silicone systems, while deviations remain in the translucent and harder formulations.

To quantitatively assess the above findings, two types of inverse design error were analysed, following the definitions in Figure 9. As summarised in Table 9, Error 1, which represents the difference between the desired target T_Y and the ReSM prediction $\hat{Y}$, is generally small. Only Ecoflex 00-31 and Ecoflex 00-45 exhibit notable discrepancies, with Y_1 Error 1 of 17% and Y_2 Error 1 of

26404567, 2026, 8, Downloaded from https://advanced.onlinelibrary.wiley.com/doi/10.1002/aisy.202501200 by Imperial College London, Wiley Online Library on [25/08/2026]. See the Terms and Conditions (https://onlinelibrary.wiley.com/terms-and-conditions) on Wiley Online Library for rules of use; OA articles are governed by the applicable Creative Commons License

TABLE 8 | Inverse design of real silicone samples.

Real sample	T_{Y_1}	T_{Y_2}	$\hat{x}_1$	$\hat{x}_2$	$\hat{x}_3$	Desirability	Design
Ecoflex 00-31	75.43 (NTB)	38.60 (STB)	18	80	2	0.7322	I_1
			19	79	2	0.7266	I_2
			17	80	3	0.7243	I_3
Ecoflex 00-45	97.23 (LTB)	44.40 (NTB)	23	77	0	0.8925	I_1
			22	78	0	0.8914	I_2
			24	76	0	0.8856	I_3
DragonSkin 20	33.13 (NTB)	70.40 (NTB)	65	16	19	0.9932	I_1
			64	17	19	0.9923	I_2
			63	18	19	0.9879	I_3
DragonSkin 30	36.23 (NTB)	75.00 (NTB)	75	8	17	0.9961	I_1
			76	7	17	0.9935	I_2
			74	9	17	0.9925	I_3
SORTA-Clear 40	84.73 (LTB)	75.20 (NTB)	77	23	0	0.9145	I_1
			76	24	0	0.9117	I_2
			75	25	0	0.9089	I_3

TABLE 9 | Inverse design performance with tailoring target from real silicone samples.

Inverse design	T_{Y_1}	$\hat{Y}_1$	R_{Y_1}	Y_1 Error 1	Y_1 Error 2	T_{Y_2}	$\hat{Y}_2$	R_{Y_2}	Y_2 Error 1	Y_2 Error 2
Ecoflex 00-31 (I_1)	75.43	74.90	82.60	0.53 (0.7%)	−7.70 (10.3%)	38.60	41.41	43.20	−2.81 (7.2%)	−1.79 (4.3%)
Ecoflex 00-31 (I_2)	75.43	74.94	81.03	0.49 (0.6%)	−6.09 (8.1%)	38.60	42.17	44.20	−3.57 (9.2%)	−2.03 (4.8%)
Ecoflex 00-31 (I_3)	75.43	72.44	79.25	2.99 (4.0%)	−6.81 (9.4%)	38.60	40.84	43.40	−2.24 (4.8%)	−2.56 (6.3%)
Ecoflex 00-45 (I_1)	97.23	80.25	79.81	16.98 (17.5%)	0.44 (0.5%)	44.40	44.74	45.80	−0.34 (0.8%)	−1.06 (2.4%)
Ecoflex 00-45 (I_2)	97.23	80.18	82.95	17.05 (17.5%)	−2.77 (3.5%)	44.40	44.00	46.00	−0.40 (0.9%)	−2.00 (4.5%)
Ecoflex 00-45 (I_3)	97.23	80.31	82.72	16.92 (17.4%)	−2.41 (3.0%)	44.40	45.47	46.40	−1.07 (2.4%)	−0.93 (2.0%)
DragonSkin 20 (I_1)	33.13	33.68	21.00	−0.55 (1.7%)	12.68 (37.6%)	70.40	70.51	65.60	−0.11 (0.2%)	4.91 (6.9%)
DragonSkin 20 (I_2)	33.13	33.84	19.14	−0.71 (2.1%)	14.70 (43.4%)	70.40	70.06	63.40	0.34 (0.5%)	6.66 (9.5%)
DragonSkin 20 (I_3)	33.13	34.00	22.70	−0.87 (2.6%)	11.3 (33.2%)	70.40	69.62	63.60	0.78 (1.1%)	6.02 (8.6%)
DragonSkin 30 (I_1)	36.23	36.54	27.39	−0.31 (0.9%)	9.15 (25.0%)	75.00	74.78	69.40	0.22 (0.3%)	5.38 (7.2%)
DragonSkin 30 (I_2)	36.23	36.40	49.14	−0.17 (0.5%)	−12.74 (35.0%)	75.00	75.16	67.80	−0.16 (0.2%)	7.36 (9.8%)
DragonSkin 30 (I_3)	36.23	36.67	48.30	−0.44 (1.2%)	−11.63 (31.7%)	75.00	74.40	68.60	−0.60 (0.8%)	5.80 (7.8%)
SORTA-Clear 40 (I_1)	84.73	83.65	82.16	1.08 (1.3%)	1.49 (1.8%)	75.20	75.18	71.20	0.02 (0.0%)	3.98 (5.3%)
SORTA-Clear 40 (I_2)	84.73	83.59	80.40	1.14 (1.3%)	3.19 (3.8%)	75.20	74.78	69.40	0.42 (0.6%)	5.38 (7.2%)
SORTA-Clear 40 (I_3)	84.73	83.53	83.53	1.20 (1.4%)	0 (0.0%)	75.20	74.38	70.60	0.82 (1.1%)	3.78 (5.1%)

5%–10%, respectively. By contrast, the predictions $\hat{Y}$ for the other inverse designs are close to their corresponding T_Y, with most errors below 1%. This is primarily because the specified T_{Y_1} of Ecoflex 00-45 and T_{Y_2} of Ecoflex 00-31 lie beyond the FPS (97.23%, Shore 00-38.60). Consequently, their desirability criteria were assigned as LTB and STB (Table 8), which inevitably results in a non-negligible gap of Error 1.

As for Error 2, it is defined as the difference between the predicted $\hat{Y}$ and the experimentally measured property R_Y of real 3D-printed samples. In terms of elastomer transoparency Y_1, Error 2 for Ecoflex 00-45 and SORTA-Clear is low (0-4%), demonstrating high predictive accuracy for elastomer transparency. Ecoflex 00-31 follows with an Error 2 of 8%–10%, which remains relatively accurate. By contrast, the DragonSkin designs, being more opaque, show substantially higher Error 2 values (25%–43%), indicating that the transparency ReSM $Y_1(x)$ performs less reliably in the opacity region compared with the clarity region. For elastomer hardness R_{Y_2}, all five materials exhibit consistently low Error 2 values, generally within 2%–10%. This suggests that the predictive performance of hardness ReSM $Y_2(x)$ is well balanced across the entire FPS.

As shown in Figure 14E, the accumulated inverse design errors of each I_1, I_2 and I_3 are compared in terms of each material. Among them, I_1 consistently exhibits the smallest total error across both Y_1 and Y_2, as its desirability is closest to the optimal inverse design (Table 8). In addition, the average inverse design error

2640567, 2026, 8, Downloaded from https://advanced.onlinelibrary.wiley.com/doi/10.1002/aisy.202501200 by Imperial College London, Wiley Online Library on [25/08/2026]. See the Terms and Conditions (https://onlinelibrary.wiley.com/terms-and-conditions) on Wiley Online Library for rules of use; OA articles are governed by the applicable Creative Commons License

across samples, combining Error 1 and Error 2, is presented in Figure 14F. For both Y_1 and Y_2, Error 2 is consistently larger than Error 1, indicating that the principal gap in inverse design for tailoring elastomer property lies between property prediction $\hat{Y}$ and real measurement R_Y of 3D-printed elastomer, rather than between the tailoring target T_Y and $\hat{Y}$, which highlights the necessary of material formulation and ReSM optimisation. From this analysis, since the largest errors are observed in transparency of DragonSkin inverse designs, it suggests that the transparency ReSM $Y_1(x)$ (Figure 7A) requires further refinement in the opacity region.

4.3 | Real Sensor Property with Inverse-Designed Elastomer

To further validate the proposed i-Tac inverse design technique, we fabricated the entire contact module of VBTS through proposed i-Tac framework, incorporating the skin, marker and lens components alongside the inverse-designed elastomers. As illustrated in Figure 15, specimens representing various established VBTS designs have been produced to demonstrate the versatility of the inverse design approach, encompassing a broad range of dimensions, configurations and elastomer properties. For this validation, we selected GelSight [4] and DIGIT [19] sensors as target, which represents the most widely used commercial VBTS products. Additionally, an in-house custom-built ViTacTip [2] is included. It features a PolyJet-printed transparent skin fabricated from Agilus30 Clear and filled with a silicone-based ultra-soft elastomer. Clearly, the aforementioned sensors cover a comprehensive range of VBTS elastomer characteristics, including geometry, dimensions and material properties. They therefore serve as an appropriate control group for validating the practicality and flexibility of the i-Tac inverse design framework in whole-sensor customisation.

In terms of above control group, four types of i-Tac specimens were fabricated: (1) flat-shaped ViTacTip (ViTacTip-f), 30 mm radius, 10 mm elastomer height, 1 mm skin thickness; (2) round-shaped ViTacTip (ViTacTip-r), 30 mm radius, 10 mm elastomer height, 1 mm skin thickness; (3) GelSight base sample (GBS), 25 mm width, 5 mm elastomer height, 0.5 mm skin thickness, no coating; and (4) DIGIT base sample (DBS), 20 mm width, 8 mm elastomer height, 0.5 mm skin thickness, no coating.

4.3.1 | Inverse Design Process

During establishing T_Y, it is impractical to measure the optical clarity on physical sensor via spectrometer. Thereby, the transparency targets T_{Y_1} are set as LTB criteria to reach maximum elastomer clarity. Then, Shore 00 durometer was employed to assess the hardness of control group via indentation on their sensor surfaces. The measured values are as follows: flat ViTacTip (homemade): 29.20, round ViTacTip (homemade): 30.20, GelSight (commercial): 70.40, and DIGIT (commercial): 76.60 (Shore 00). Based on upon results, two sets of i-Tac inverse design targets were subsequently formulated: (1) The first target utilises pure GM design (GM10, see Table 3) as a gel-like elastomer to realise an ultra-soft silicone in ViTacTip with moderate optical clarity. (2) The second set adopts the same formulation as SORTA-Clear's I3 ((x_1, x_2, x_3)=(75,25,0), Table 8), wherein T_{Y_1} adheres to LTB criterion and T_{Y_2} targets a

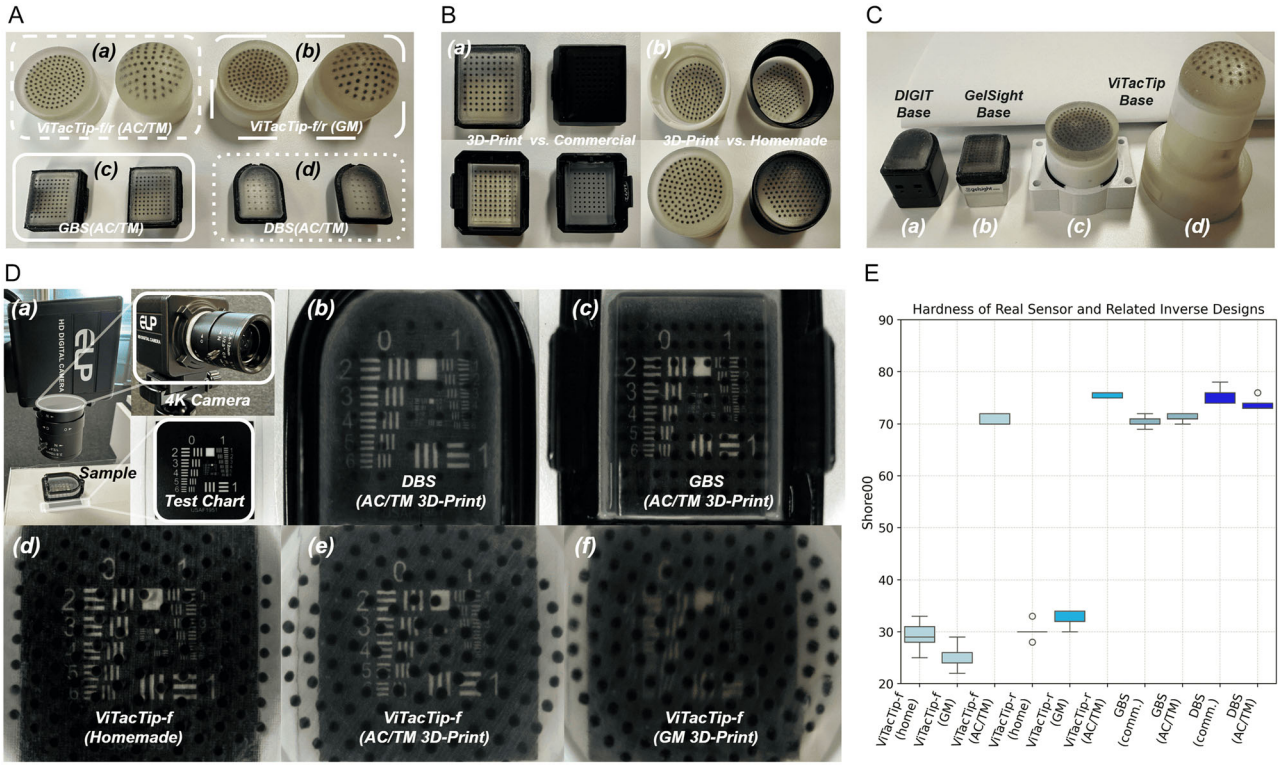


FIGURE 15 | (A) (a) ViTacTip-f/r with AC/TM elastomer, (b) ViTacTip-f/r with pure GM elastomer, (c) GBS with AC/TM elastomer, (d) DBS with AC/TM elastomer. (B) (a) Comparison between 3D-printed GBS and commercial GelSight; (b) comparison between 3D-printed and homemade ViTacTip-f. (C) VBTS base mounted with 3D-printed contact modules, (a) DIGIT base, (b) GelSight base, (c/d) ViTacTip base v1/v2. (D) (a) Experiment setup of optical resolution using 4K camera and USAF 1951 test chart. (b/c) Observed images for 3D-printed GBS/DBS. (d–f) Observed images for homemade/3D-printed ViTacTip-f. (E) Hardness comparison between real sensor samples.

26404567, 2026, 8, Downloaded from https://advanced.onlinelibrary.wiley.com/doi/10.1002/aisy.202501200 by Imperial College London, Wiley Online Library on [25/08/2026]. See the Terms and Conditions (https://onlinelibrary.wiley.com/terms-and-conditions) on Wiley Online Library for rules of use; OA articles are governed by the applicable Creative Commons License

Shore 00 hardness of 75.20 (Table 9); both values align with the properties of GelSight and DIGIT. Accordingly, AC/TM(75/25) mixture design was selected for the inverse design targeting GelSight and DIGIT. This material was also used to fabricate a ViTacTip for comparison with the pure GM variant. The comparison between resulting i-Tac products alongside commercial and homemade control group is illustrated in Figure 15A–C.

4.3.2 | Optical Transparency

In Figure 15 D.a, a 4K camera and a USAF 1951 resolution test chart[7] are employed to evaluate the optical clarity. The test chart comprises numerous small target patterns featuring a graded series of precise spatial frequency elements. The smallest distinguishable element under acceptable image contrast conditions provides an estimate of the resolution limit. Each sensor sample is placed directly above the test chart, and the finest resolvable element is identified by its group (G) and element (E) indices based on the image captured by the 4K camera. These indices are used to determine the corresponding spatial frequency in line pairs per millimetre (lp/mm), which serves as a quantitative measure of the optical resolution (R) of the sensor sample:

$$R(\mathrm{lp/mm}) = 2^{\mathrm{G}+(\mathrm{E}-1)/6} \tag{17}$$

In this manner, the optical transparency of above sensors can be quantified by comparing the optical resolution with and without the sample in place. To ensure a fair comparison, only flat-shaped designs were selected (Figure 15 D.b–f), which can maintain consistent contact with the test chart, thereby ensuring valid imaging with clearly discernible pattern elements. The measured optical resolutions are summarised in Table 10. The highest resolution, measured without any sample, is 12.70 lp/mm. As a baseline, the homemade flat ViTacTip achieved a resolution of 5.04 lp/mm. The 3D-printed ViTacTip filled with AC/TM attained 3.56 lp/mm, slightly lower than the baseline, whereas the version with pure GM reached only 1.0 lp/mm. This reduction in clarity for the pure GM sample can be attributed to two main factors: (1) firstly, GM exhibits approximately 20% lower inherent transparency than the AC/TM mixture; (2) secondly, GM provides inferior structural support for the overlying lens during printing, potentially introducing optical aberrations. These issues may be mitigated through structural optimisations, such as reducing the thickness of the elastomer or the span of the lens. In contrast, sensors fabricated with AC/TM demonstrate superior optical performance. For instance, the 3D-printed GBS and DBS achieved resolutions between 4.49 and 5.04 lp/mm.

4.3.3 | Mechanical Hardness

As summarised in Figure 15E, the 3D-printed ViTacTip (GM) exhibit Shore 00 hardness values of 25.40 and 32.40, which are comparable to the handmade ViTacTip (29.20, 30.20) and significantly lower than the AC/TM ViTacTip (70.80, 75.60). These results indicate that the pure GM material extends the FPS of i-Tac inverse design into the ultra-soft range (Shore 00-20 to 00-40), enabling the fabrication of sensor designs that demand high mechanical ductility and shear sensitivity. In addition, other two AC/TM-based i-Tac products exhibit hardness values within the Shore 00-70 to 00-75 range, consistent with the AC/TM ViTacTip. For instance, the AC/TM GBS and DBS show hardness values of 71.20 and 73.80, respectively, aligning closely with their commercial control group of GelSight/DIGIT (70.40, 76.60).

The above evaluation results demonstrate that i-Tac inverse-designed product can not only construct the entire VBTS contact modules of various design geometry via monolithic manufacturing with high fabrication convenience but also match the material property of handmade/commercial sensor upon both optical clarity and mechanical hardness under suitable architecture design.

5 | Discussion

Despite the promising performance of the proposed i-Tac framework, several limitations remain. For example, the current ReSMs are trained on 16 mixture design samples, which may limit modelling accuracy in sparsely sampled regions of the composition space. Future work will explore denser material calibration and data-efficient surrogate models (e.g., Bayesian approaches) to improve predictive robustness.

Also, the biomimetic inspiration in this work should be interpreted primarily at the conceptual level rather than as a full mechanical replication of human skin. Specifically, the proposed mixture design targets the intrinsic material properties of elastomeric micro-elements (material voxels), capturing the constituent-level property blending that also underlies dermal tissue, where collagen, elastin and ground substance collectively determine baseline material behaviour. We acknowledge that real skin exhibits pronounced anisotropy, viscoelasticity and layered organisation arising from higher-order structural arrangements across multiple scales. The present study focuses on the material composition dimension as a foundational step. Importantly, this material-level tuneability provides an enabling basis for future structural-mechanical co-design, where anisotropic responses may be achieved through the spatial organisation of mixture-designed voxels. In this context, recent multi-material topology optimisation studies have highlighted the advantages of jointly optimising material distribution and structural layout, rather than treating material selection and geometry as separate design problems. For example, recent work on ultra-soft magneto-active structures [30] demonstrates that such optimisation can be further enhanced

TABLE 10 | Optical resolution of real sensor samples.

Parameter	No sample	ViTacTip-f homemade	ViTacTip-f, AC/TM	ViTacTip-f, GM	GBS, AC/TM	DBS, AC/TM
Elastomer height (mm)	-	5	10	10	6	8
Group (G)	3	2	1	0	2	2
Element (E)	5	3	6	1	3	2
Optical resolution (lp/mm)	12.70	5.04	3.56	1.00	5.04	4.49

26404567, 2026, 8, Downloaded from https://advanced.onlinelibrary.wiley.com/doi/10.1002/aisy.202501200 by Imperial College London, Wiley Online Library on [25/08/2026]. See the Terms and Conditions (https://onlinelibrary.wiley.com/terms-and-conditions) on Wiley Online Library for rules of use; OA articles are governed by the applicable Creative Commons License

by explicitly incorporating constitutive descriptions of the underlying coupled physical behaviour into the design process. More broadly, this points towards a physics-informed co-design paradigm that integrates both material and structural design. Although beyond the scope of this work, we believe this represents a promising direction for future research.

Furthermore, the proposed i-Tac framework is inherently extensible beyond the specific material set used in this study. In particular, the mixture design formulation can naturally evolve alongside ongoing iterations of PolyJet printable materials. As new resins with improved optical or mechanical performance become available, they can be incorporated into the mixture space to progressively expand the feasible material property range and further enhance inverse design fidelity. Beyond PolyJet technology, the underlying design philosophy of i-Tac is also applicable to other multi-material fabrication paradigms (e.g., DIW-based printing). In such cases, the framework can be transferred with minimal modification by redefining the material coordinate system in the MDS and re-fitting the ReSM using the corresponding experimental data, while preserving the desirability-driven optimisation strategy. This adaptability highlights the long-term scalability and cross-platform potential of the proposed inverse design pipeline for VBTS elastomer engineering.

6 | Conclusion

This study presents i-Tac, an inverse design methodology for 3D-printed elastomers with tailored optical transparency and hardness, aiming to enhance the monolithic fabrication of VBTSs through improved design flexibility and end-product quality. Inspired by the hierarchical structure of human skin, where collagen fibres, elastic fibres and ground substance jointly determine mechanical behaviour, we propose a material mixture design framework comprising three PolyJet materials: AC, TM and GM. Within this mixture space, a systematic set of samples is fabricated and characterised to establish the material formulation landscape. Two ReSMs are subsequently developed, demonstrating that the proposed mixture design achieves a wide dynamic range in both optical and mechanical properties, which is critical for VBTS design and fabrication. Given target material specifications, a desirability function–based strategy is introduced to address the multi-objective trade-off between transparency and hardness. The resulting theoretical optimum is further translated into a practical operating window, yielding manufacturable mixture compositions that can be directly realised via monolithic 3D printing and thereby completing the end-to-end inverse design pipeline.

To validate the effectiveness of the proposed i-Tac framework, comprehensive experiments were conducted, including material characterisation, theoretical analysis, fabricated sample evaluation and functional VBTS performance assessment. The results demonstrate that, compared with conventional PolyJet materials, the proposed mixture elastomers substantially expand the achievable property space while narrowing the performance gap between 3D-printed elastomers and commercial silicones. Moreover, the combined use of response surface modelling and desirability optimisation enables accurate translation from target properties in the FPS to optimal material compositions. The framework was further employed to replicate the properties of representative commercial silicone elastomers by treating their characteristics as design targets, with the resulting samples exhibiting high property fidelity. Finally, the method demonstrates strong property adaptability at the level of complete VBTS contact modules, successfully matching the characteristics of both custom-built and commercial sensors.

Overall, the proposed i-Tac inverse design framework provides a practical and flexible pathway for fabricating VBTS elastomers with tuneable optical and mechanical properties. This work lays an important foundation for advancing monolithic 3D printing of VBTS and for further exploration of high-performance tactile sensing systems.

Author Contributions

Wen Fan: conceptualisation (lead), data curation (lead), formal analysis (lead), investigation (lead), methodology (lead), software (lead), validation (lead), visualisation (lead), writing – original draft (lead). **Dandan Zhang:** funding acquisition (lead), project administration (lead), resources (lead), supervision (lead), writing – review and editing (lead).

Funding

This work was supported by University Postgraduate Programme.

Conflicts of Interest

The authors declare no conflicts of interest.

Data Availability Statement

The data that support the findings of this study are available from the corresponding author upon reasonable request.

Endnotes

[1] https://www.stratasys.com/en/materials/materials-catalog/polyjet-materials/agilus30/

[2] https://www.stratasys.com/en/materials/materials-catalog/polyjet-materials/tissuematrix/

[3] https://www.stratasys.com/en/materials/materials-catalog/polyjet-materials/gelmatrix/

[4] https://www.smooth-on.com/product-line/ecoflex/

[5] https://www.smooth-on.com/product-line/dragon-skin/

[6] https://www.smooth-on.com/product-line/sorta-clear/

[7] https://en.wikipedia.org/wiki/1951_USAF_resolution_test_chart

References

1. S. Zhang, Z. Chen, Y. Gao, et al., "Hardware Technology of Vision-Based Tactile Sensor: A Review," *IEEE Sensors Journal* 22, no. 22 (2022): 21410–21427.

2. W. Fan, H. Li, W. Si, S. Luo, N. Lepora, and D. Zhang, "Vitactip: Design and verification of a novel biomimetic physical vision-tactile fusion sensor," in *2024 IEEE International Conference on Robotics and Automation (ICRA)*, (IEEE, 2024), 1056–1062.

3. W. Fan, H. Li, and D. Zhang, "Crystaltac: Vision-Based Tactile Sensor Family Fabricated via Rapid Monolithic Manufacturing," *Cyborg and Bionic Systems* 6 (2025): 0231.

26404567, 2026, 8, Downloaded from https://advanced.onlinelibrary.wiley.com/doi/10.1002/aisy.202501200 by Imperial College London, Wiley Online Library on [25/08/2026]. See the Terms and Conditions (https://onlinelibrary.wiley.com/terms-and-conditions) on Wiley Online Library for rules of use; OA articles are governed by the applicable Creative Commons License

4. W. Yuan, S. Dong, and E. H. Adelson, "Gelsight: High-Resolution Robot Tactile Sensors for Estimating Geometry and Force," *Sensors* 17, no. 12 (2017): 2762.

5. D. Zhang, W. Fan, J. Lin, et al., "Design and Benchmarking of a Multimodality Sensor for Robotic Manipulation with Gan-Based Cross-Modality Interpretation," *IEEE Transactions on Robotics* 41 (2025): 1278–1295.

6. D. F. Gomes, Z. Lin, and S. Luo, "Geltip: A finger-shaped optical tactile sensor for robotic manipulation," in *2020 IEEE/RSJ international conference on intelligent robots and systems (IROS)*, (IEEE, 2020), 9903–9909.

7. C. Lin, H. Zhang, J. Xu, L. Wu, and H. Xu, "9dtact: A Compact Vision-Based Tactile Sensor for Accurate 3d Shape Reconstruction and Generalizable 6d Force Estimation," *IEEE Robotics and Automation Letters* 9, no. 2 (2023): 923–930.

8. Q. Cong, S. Oh, W. Fan, S. Luo, K. Althoefer, and D. Zhang, "Taceva: A Performance Evaluation Framework for Vision-Based Tactile Sensors," *Advanced Intelligent Systems* 8 (2025): e202501179.

9. S. Zhang, Y. Sun, J. Shan, et al., "Tirgel: A Visuo-Tactile Sensor with Total Internal Reflection Mechanism for External Observation and Contact Detection," *IEEE Robotics and Automation Letters* 8, no. 10 (2023): 6307–6314.

10. J. Di, Z. Dugonjic, W. Fu, et al., "Using Fiber Optic Bundles to Miniaturize Vision-Based Tactile Sensors," *IEEE Transactions on Robotics* 41 (2024): 62–81.

11. A. Solayman, M. Halwani, I. M. Zaid, et al., "Mechanical Behaviour, Contact Pose Estimation, and Finite Element Analysis of Vision Based Tactile Sensors Fabricated by Molding and Direct Ink Writing: A Comparative Study," *Advanced Engineering Materials* 26, no. 22 (2024): 2400630.

12. W. Fan, H. Li, Y. Xing, and D. Zhang, "Design and Evaluation of a Rapid Monolithic Manufacturing Technique for a Novel Vision-Based Tactile Sensor: C-Sight," *Sensors* 24, no. 14 (2024): 4603.

13. W. Fan, H. Li, and D. Zhang, "Magictac: A novel high-resolution 3d multi-layer grid-based tactile sensor," in *2024 IEEE International Conference on Robotics and Automation (ICRA)*, (IEEE, 2024), 388–394.

14. L. Willemet, *The Biomechanics of the Tactile Perception of Friction* (Springer, 2022).

15. J. A. Cornell, "A Retrospective View of Mixture Experiments," *Quality Engineering* 23, no. 4 (2011): 315–331.

16. A. I. Khuri and S. Mukhopadhyay, "Response Surface Methodology," *Wiley Interdisciplinary Reviews: Computational Statistics* 2, no. 2 (2010): 128–149.

17. N. R. Costa, J. Lourenço, and Z. L. Pereira, "Desirability Function Approach: A Review and Performance Evaluation in Adverse Conditions," *Chemometrics and Intelligent Laboratory Systems* 107, no. 2 (2011): 234–244.

18. G. Zhang, Y. Du, H. Yu, and M. Y. Wang, "Deltact: A Vision-Based Tactile Sensor Using a Dense Color Pattern," *IEEE Robotics and Automation Letters* 7, no. 4 (2022): 10778–10785.

19. M. Lambeta, P.-W. Chou, S. Tian, et al., "Digit: A Novel Design for a Low-Cost Compact High-Resolution Tactile Sensor with Application to in-Hand Manipulation," *IEEE Robotics and Automation Letters* 5, no. 3 (2020): 3838–3845.

20. X.-Q. Han, X.-D. Wang, M.-Y. Xu, et al., "Ai-Driven Inverse Design of Materials: Past, Present, and Future," *Chinese Physics Letters* 42, no. 2 (2025): 027403.

21. W. L. Ng, G. L. Goh, G. D. Goh, J. S. J. Ten, and W. Y. Yeong, "Progress and Opportunities for Machine Learning in Materials and Processes of Additive Manufacturing," *Advanced Materials* 36, no. 34 (2024): 2310006.

22. C. S. Ha, D. Yao, Z. Xu, et al., "Rapid Inverse Design of Metamaterials Based on Prescribed Mechanical Behavior through Machine Learning," *Nature Communications* 14, no. 1 (2023): 5765.

23. Z. Chai, Z. Zong, H. Yong, et al., "Tailoring Stress–strain Curves of Flexible Snapping Mechanical Metamaterial for on-Demand Mechanical Responses via Data-Driven Inverse Design," *Advanced Materials* 36, no. 33 (2024): 2404369.

24. A. E. Allen and A. Tkatchenko, "Machine Learning of Material Properties: Predictive and Interpretable Multilinear Models," *Science Advances* 8, no. 18 (2022): eabm7185.

25. R. McLean and V. Anderson, "Extreme Vertices Design of Mixture Experiments," *Technometrics* 8, no. 3 (1966): 447–454.

26. Y. Gao, B. Yu, S. Xin, et al., "Use of Extreme Vertices Method for Analysis of How Proportional Composition Affects Component Interactions and Product Distribution during Hydrothermal Treatment," *BioResources* 11, no. 2 (2016): 4899–4920.

27. H. Zhang, Z. Liu, S. Yin, and H. Xu, "A Hybrid Multi-Objective Optimization of Functional Ink Composition for Aerosol Jet 3d Printing via Mixture Design and Response Surface Methodology," *Scientific Reports* 13, no. 1 (2023): 2513.

28. D. F. Swinehart, "The Beer-Lambert Law," *Journal of Chemical Education* 39, no. 7 (1962): 333.

29. J. A. Cornell, "The Fitting of Scheffé-Type Models for Estimating Solubilities of Multisolvent Systems," *Journal of Biopharmaceutical Statistics* 1, no. 2 (1991): 303–329.

30. C. Perez-Garcia, R. Ortigosa, J. Martínez-Frutos, and D. Garcia-Gonzalez, "Topology and Material Optimization in Ultra-Soft Magneto-Active Structures: Making Advantage of Residual Anisotropies," *Advanced Materials* (2025): e18489.

Appendix

A. Material Property Evaluation Details

1. Hardness: For elastomers, softness is a key material attribute that distinguishes them from rigid solids. In tactile sensing applications, an elastomer with appropriate compliance can respond effectively to contact stimuli through measurable surface deformation. Hardness is commonly used as a quantitative metric (the inverse of softness), describing the resistance of a material to indentation or local deformation and reflecting its resistance to permanent damage such as scratching, indentation, or cutting. In this work, an indentation-based Shore 00 hardness test is performed using a durometer to characterise the elastomers. During testing, the durometer was used to uniformly collect at least five data readings from the surface of each sample.

As summarised in Table 6, the measured hardness values of the 21 materials span approximately 20−85 Shore 00 (very soft to soft). Among the 3D-printed materials, pure AC exhibits the highest stiffness, with an experimentally measured hardness of 84.8 Shore 00 (manufacturer specification, Shore A 30). As the TM proportion in the AC/TM mixtures increases to 80%, the hardness decreases proportionally to 43.2 Shore 00, indicating a substantial softening effect. A similar trend is observed in the GM/AC mixtures, although the softening occurs more rapidly, reaching 44.8 Shore 00 at 60% GM. When AC is removed entirely, the TM/GM mixtures further reduce the hardness to approximately 20−30 Shore 00, corresponding to extremely compliant materials.

In the ternary AC/TM/GM mixtures, the hardness variation becomes more moderate due to the coupled material interactions. The multi-layer grid (SUP) sample exhibits a hardness of 68 Shore 00, representing a clear reduction from pure AC and comparable to AC6/TM4 and AC5/TM2/GM2.

For comparison, the five mould-cast silicones fall within the range of approximately 40−75 Shore 00, largely overlapping with the 3D-printed mixture designs. Ecoflex 00-31 and 00-45 are the softest (38.6/44.4 Shore 00), comparable to AC2/TM2/GM5 and GM6/AC4, respectively. DragonSkin 20 is significantly stiffer (approximately 70 Shore 00), similar to the SUP, while DragonSkin 30 and SORTA-Clear 40 further increase to around 75 Shore 00, positioned between AC8/TM2 and pure AC.

26404567, 2026, 8, Downloaded from https://advanced.onlinelibrary.wiley.com/doi/10.1002/aisy.202501200 by Imperial College London, Wiley Online Library on [25/08/2026]. See the Terms and Conditions (https://onlinelibrary.wiley.com/terms-and-conditions) on Wiley Online Library for rules of use; OA articles are governed by the applicable Creative Commons License

Overall, the results indicate that the proposed 3D-printed mixture designs can achieve softness levels comparable to mainstream PolyJet elastomers, such as AC, while offering flexible hardness tuneability through compositional control comparative to mould-cast silicones.

2. Poisson's Ratio: Poisson's ratio v is a fundamental mechanical parameter describing the relationship between transverse strain $\varepsilon_{\text{trans}}$ and axial strain $\varepsilon_{\text{axial}}$ under uniaxial loading. In tactile sensing applications, near-incompressibility ($v = 0.5$) implies that geometric deformation under external loading occurs with limited volume variation.

$$v = -\frac{d\varepsilon_{\text{trans}}}{d\varepsilon_{\text{axial}}} \tag{A1}$$

In this study, Poisson's ratio is estimated using digital image correlation (DIC). During uniaxial tensile testing, surface markers applied to ASTM D412 dog-bone specimens are tracked to obtain full-field displacement data. Axial and transverse strains are then extracted from the measured marker displacements, from which v is calculated. Although DIC provides a non-contact and spatially resolved strain measurement approach, its finite spatial resolution and sensitivity to surface texture, illumination conditions and speckle quality may introduce uncertainty. Consequently, the experimentally obtained Poisson's ratios may deviate from their theoretical values.

As summarised in Table 6, the measured Poisson's ratios of the 21 samples range from 0.35 to 0.45. For the 3D-printed elastomers, most values fall within 0.40–0.45, approaching the commonly assumed incompressible limit and indicating relatively low volumetric compressibility. By comparison, the mould-cast silicones exhibit measured values between 0.35 and 0.40, whereas their nominal Poisson's ratios are typically reported in the range of 0.47–0.50. This systematic underestimation is primarily attributed to DIC-related measurement uncertainty and practical material variability. Importantly, both the 3D-printed mixture designs and the mould-cast silicones are evaluated using the same DIC setup and processing pipeline; therefore, the relative comparison between the two material groups remains valid. Under this consistent measurement framework, the mixture-designed elastomers demonstrate measured incompressibility that is comparable to, and in most cases slightly higher than, that of the commercial silicones.

3. Uniaxial Tensile Experiment: Uniaxial tensile testing is widely used to characterise the mechanical behaviour of elastomers under unidirectional loading. Its primary objective is to obtain stress–strain curves for analysing tensile properties such as elastic modulus and tensile hysteresis. ASTM D412 is a well-established standard for evaluating the tensile properties of elastomers, specifying specimen geometry, testing conditions and reporting procedures. For VBTS tactile sensing, shear contact dynamic is closely related to the material tensile property. The tensile test results are presented in Figure 12A.

- **Monotonic Tensile Loading:** Figure 12A.a shows the stress σ-strain ε responses of the 21 elastomers under monotonic loading from 0 to 100% strain. Most materials exhibit approximately linear behaviour within this range; however, AC displays noticeable nonlinearity. Specifically, the stress of AC increases rapidly up to approximately 10% strain, after which the growth rate gradually decreases and becomes nearly linear beyond 20% strain. AC also consistently exhibits higher stress levels than the other materials throughout the loading process. The stress–strain curves of the remaining mixture-designed elastomers generally fall within the envelope defined by the mould-cast silicones. To quantify tensile stiffness, the engineering stress at 100% strain is used to approximate the elastic modulus E (Young's modulus), which characterises the material resistance to tensile deformation. Due to minor measurement fluctuations near 100% strain, the peak stress immediately prior to the fluctuation is adopted as the representative value of E.

$$E = \frac{\sigma_{100\%}}{\varepsilon_{100\%}} = \sigma_{100\%} \tag{A2}$$

  As summarised in Table 6, the elastic modulus of the 21 materials spans approximately 48-450 kPa, representing nearly an order-of-magnitude variation. Consistent with Figure 12A.a, the traditional PolyJet material AC, exhibits the highest modulus (449.87 kPa), approximately 70% higher than the SUP (270 kPa). In comparison, for the 3D-printed mixture designs, both AC/TM and GM/AC elastomers show a gradual reduction in modulus from approximately 230 kPa to 130 kPa as the AC fraction decreases from 80%. While TM/GM mixtures occupy a substantially lower range (approximately 80-90 kPa), corresponding to roughly one-fifth of the stiffness of pure AC. What's more, the mould-cast silicones are distributed across three characteristic levels: approximately 330 kPa (SORTA-Clear 40), 235 kPa (DragonSkin 20) and about 50 kPa (Ecoflex). Notably, the softest 3D-printed materials has closely reached commercial silicone through the lowest modulus observed from mixture designs.

- **Cyclic Tensile Loading**: Cyclic tensile tests are conducted to evaluate tensile hysteresis, which reflects the internal energy dissipation between loading and unloading within a stretch cycle. The hysteresis is quantified by the normalised area difference between the loading and unloading stress-strain curves. A larger ratio indicates greater energy dissipation and more pronounced viscoelastic effects.

$$H = \frac{A_{\text{load}} - A_{\text{unload}}}{A_{\text{load}}} \tag{A3}$$

  The quantitative results in Table 6 indicates that the tensile hysteresis of AC and the SUP reach 0.64 and 0.33, respectively. For the mixture-designed elastomers, hysteresis generally decreases with reduced AC content. Most mixtures containing less than 40% AC achieve hysteresis values below 0.1, comparable to those of the mould-cast silicones.

- **Combined Tensile Performance:** The combined relationship of elastic modulus and tensile hysteresis is illustrated in Figure 12A.b. AC occupies the upper-right region of the plot, characterised by both high stiffness and high energy dissipation, indicating strong load resistance but relatively slow dynamic response. The SUP follows a similar trend but with both metrics reduced to approximately half of those of pure AC. For the remaining 3D-printed mixture designs, the AC/TM mixtures show an approximately proportional relationship between AC content and both modulus and hysteresis, forming a near-linear distribution. In GM/AC mixtures, a similar scaling trend is evident primarily in the elastic modulus, whereas the hysteresis values cluster within the range of 0.2-0.3. TM/GM mixtures exhibit substantially reduced modulus ($\lesssim$100 kPa) and hysteresis ($\lesssim$0.1), indicating rapid response but without a clear linear trend. The ternary AC/TM/GM mixtures demonstrate tensile behaviour comparable to representative AC/TM compositions (e.g., AC2/TM8 and AC4/TM6). By comparison, the mould-cast silicones show a more horizontally distributed pattern, suggesting that they can provide a wide stiffness range while maintaining relatively stable hysteresis. In contrast, the tensile performance of the 3D-printed elastomers remains partly constrained by the intrinsic viscoelastic characteristics of AC, such that achieving higher stiffness tends to be accompanied by increased hysteresis. However, from a comparative perspective, mixture design demonstrates a marked improvement in tensile material properties relative to conventional PolyJet materials such as AC and SUP.

4. Uniaxial Compressive Experiment: In practical tactile sensing scenarios, the dominant loading mode is compression, as normal force is required to establish effective contact. Consequently, the elastomer layer of the tactile sensor primarily undergoes compressive deformation during operation. Understanding the compressive behaviour of candidate materials is therefore essential for sensor design and performance optimisation. ASTM D575 provides a standardised protocol for evaluating the compressive properties of rubber and elastomeric materials under uniaxial loading, and is adopted here to characterise both 3D-printed and mould-cast elastomers. The experimental results are presented in Figure 12B.

26404567, 2026, 8, Downloaded from https://advanced.onlinelibrary.wiley.com/doi/10.1002/aisy.202501200 by Imperial College London, Wiley Online Library on [25/08/2026]. See the Terms and Conditions (https://onlinelibrary.wiley.com/terms-and-conditions) on Wiley Online Library for rules of use; OA articles are governed by the applicable Creative Commons License

- **Monotonic Compression:** Figure 12B.a shows the stress–strain responses under monotonic compression up to 20% strain. Unlike the tensile results, DragonSkin 30 defines the upper boundary of the response envelope rather than AC. The two materials exhibit similar behaviour below approximately 5% strain; however, with increasing compression depth, DragonSkin 30 demonstrates a noticeably steeper stress growth than AC. SORTA-Clear 40 and DragonSkin 20 follow trends similar to DragonSkin 30 and AC, respectively, and both exceed the stress of AC beyond approximately 15% strain. The remaining materials exhibit more gradual stress increases, with TM/GM mixtures forming the lower boundary of the response range. To quantify compressive stiffness, the engineering stress at 10% strain is defined as the compressive modulus, as summarised in Table 6. The mould-cast silicones show generally higher compressive modulus values, forming two characteristic bands (approximately 35–50 kPa and 170–230 kPa). In contrast, the 3D-printed mixture designs span a broader but overall lower range (approximately 7–150 kPa), indicating reduced resistance to compressive loading. This demonstrates that in VBTS tactile sensing, mixture design elastomers can provide force sensitivity comparable to that of mould-cast silicone.

- **Cyclic Compression:** Cyclic compression tests are performed to evaluate compressive hysteresis, which characterises the energy dissipation during loading-unloading cycles. As with the tensile case, hysteresis is quantified by the normalised area difference between the loading and unloading curves. The quantitative results in Table 6 shows that AC exhibits pronounced compressive hysteresis despite its moderate compressive modulus, indicating substantial viscoelastic energy dissipation and relatively slow recovery dynamics. Similarly, AC8/TM2 reach hysteresis values of approximately 0.5, followed by AC6/TM4, TM8/GM2 and GM4/AC6 at around 0.4 and AC4/TM6, GM6/AC4 and GM2/AC8 at approximately 0.37. In comparison, most of the remaining 3D-printed mixtures and the mould-cast silicones fall within the range of 0.15−0.30, indicating faster dynamic recovery than typical PolyJet material, AC.

- **Combined Compressive Performance:** The combined relationship of compressive modulus and hysteresis is illustrated in Figure 12B.b. Overall, clear differences are observed between the 3D-printed and mould-cast elastomers. The 3D-printed materials generally occupy a lower modulus region (below approximately 150 kPa) but exhibit a wider hysteresis spread (approximately 0.1-0.5). Within the mixture designs, the AC and TM fractions in AC/TM and TM/GM systems show observable correlations with compressive behaviour, whereas the influence of GM is less pronounced. By contrast, the mould-cast elastomers extend to higher compressive modulus values (up to approximately 230 kPa) while maintaining relatively stable hysteresis (0.1-0.25). This suggests that commercial silicones may be more suitable for applications requiring high compressive stiffness (e.g., DragonSkin and SORTA-Clear), but also with lower normal force sensitivity. For applications favouring lower compressive modulus, the 3D-printed mixture designs can achieve dynamic responses comparable to Ecoflex while offering flexible property tailoring (e.g., AC/TM/GM, TM4/GM6 and AC2/TM8).

2640567, 2026, 8, Downloaded from https://advanced.onlinelibrary.wiley.com/doi/10.1002/aisy.202501200 by Imperial College London, Wiley Online Library on [25/08/2026]. See the Terms and Conditions (https://onlinelibrary.wiley.com/terms-and-conditions) on Wiley Online Library for rules of use; OA articles are governed by the applicable Creative Commons License